RSC Advances

PAPER

View Article Online
View Journal | View Issue



Cite this: *RSC Adv.*, 2024, **14**, 3104

# Effective retention of cesium ions from aqueous environment using morphologically modified kaolinite nanostructures: experimental and theoretical studies†

Ashour M. Ahmed,*[ab] Nourhan Nasser,[cd] M. Abdel Rafea[a] and Mostafa R. Abukhadra *[cd]

Kaolinite can undergo a controlled morphological modification process into exfoliated nanosilicate sheets (EXK) and silicate nanotubes (KNTs). The modified structures were assessed as potential effective adsorbents for the retention of $Cs^+$ ions. The impact of the modification process on the retention properties was assessed based on conventional and advanced equilibrium studies, considering the related steric and energetic functions. The synthetic KNTs exhibit a retention capacity of 249.7 mg $g^{-1}$ as compared to EXK (199.8 mg $g^{-1}$), which is significantly higher than raw kaolinite (73.8 mg $g^{-1}$). The kinetic modeling demonstrates the high effectiveness of the pseudo-first-order kinetic model ($R^2$ > 0.9) to illustrate the sequestration reactions of $Cs^+$ ions by K, EXK, and KNTs. The enhancement effect of the modification processes can be illustrated based on the statistical investigations. The presence of active and vacant receptors enhanced greatly from 19.4 mg $g^{-1}$ for KA to 40.8 mg $g^{-1}$ for EXK and 46.9 mg $g^{-1}$ for KNTs at 298 K. This validates the significant impact of the modification procedures on the specific surface area, reaction interface, and reacting chemical groups' exposure. This also appeared in the enhancement of the reactivity of their surfaces to be able to uptake 10 $Cs^+$ ions by KNTs and 5 ions by EXK as compared to 4 ions by kaolinite. The thermodynamic and energetic parameters (Gaussian energy < 8.6 kJ $mol^{-1}$; uptake energy < 40 kJ $mol^{-1}$) show that the physical processes are dominant, which have spontaneous and exothermic properties. The synthetic EXK and KNT structures validate the high elimination performance of the retention of $Cs^+$ either in the existence of additional anions or cations.

Received 12th December 2023
Accepted 11th January 2024

DOI: 10.1039/d3ra08490f

rsc.li/rsc-advances



## 1 Introduction

The chemical contamination of freshwater supplies and the subsequent detrimental effects on people's health and ecosystems are significant issues that pose a serious threat to the future well-being of humanity.[1] The unregulated, widely distributed, and continued release of contaminated effluents associated with mineral extraction, agricultural activities, and industrial operations constitutes the primary origins and factors that trigger the issue of water quality contamination and its associated environmental side impacts.[2,3] The presence of toxic metals inside water bodies, either as dissolved ions or chemical complexes with other substances, poses a significant risk to the ecological integrity and well-being of humans.[2,4] These pollutants were classified as extremely toxic, non-biodegradable, and tumor-causing agents that have a tendency for accumulation inside both human and animal bodies.[4,5] The mining industry, industrial operations, and nuclear fuel manufacturing are significant contributors to various harmful and radioactive ions of metal, such as uranium, cesium, strontium, thorium, and barium.[6–8] Cesium, in its ionized form, has been categorized as an extremely toxic contaminant that is frequently emitted from many industrial processes.[9,10]

Cesium, particularly the radioactive isotope $^{137}Cs$, possesses significant importance and has substantial utilization in nuclear power plants.[11–13] This element is employed in the generation of nuclear power as a constituent in the fission processes of uranium and is released throughout the surrounding atmosphere during nuclear applications, handling of the radioactive residue, and waste disposal.[10,11,14] Cesium, when present in its radioactive form as $^{137}Cs$, demonstrates very

[a]*Physics Department, College of Science, Imam Mohammad Ibn Saud Islamic University (IMSIU), Riyadh 11623, Kingdom of Saudi Arabia*

[b]*Nanophotonics and Applications Lab, Physics Department, Faculty of Science, Beni-Suef University, Beni-Suef 62514, Egypt*

[c]*Geology Department, Faculty of Science, Beni-Suef University, Beni Suef City, Egypt. E-mail: Abukhadra89@Science.bsu.edu.eg; Tel: +20-1288447189*

[d]*Materials Technologies and Their Applications Lab, Faculty of Science, Beni-Suef University, Beni Suef City, Egypt*

† Electronic supplementary information (ESI) available. See DOI: https://doi.org/10.1039/d3ra08490f

long half-life of about 30 years and generates stream of gamma rays.[15,16] Consequently, the infiltration of these ions into reservoirs of freshwater has further exacerbated the extent of destruction of the environment along with health issues due to its notable characteristics, including its remarkable solubility, high bioavailability, low hydrated radius, high mobility, and considerable capacity for accumulation within various ecosystems in addition to the food chain, as well as its serious toxicity to humans.[7,11,15] The gamma-ray radiation has been found to have carcinogenic effects and harmful impacts on both the natural environment and people's health.[11,17,18] Cesium contamination has been linked to cancers of the kidney, liver, bladder, and thyroid gland.[16] Furthermore, because of the similarity in the physicochemical properties of $^{137}Cs$ to monovalent alkali metals, traditional and common methods of remediation such as solvent extraction, precipitation, electrodialysis, and ion exchange are ineffective in eliminating cesium pollutants.[19]

The utilization of novel adsorbents for the highly effective decontamination of cesium ions has been suggested and recommended as a relatively simple, recyclable, and economically feasible approach.[15] The adsorbents that have been recently investigated for the elimination of cesium involve ZIF-8,[13] magnetic zeolite,[16] biotite,[15] polymer–metal oxide,[20] calcium-silicate-hydrate,[21] synthetic zeolite,[22] ferrocyanide/Al-MCM-41,[23] and natural zeolite.[24] The cost of manufacture, practicality of fabrication, recyclable potential, availability, adsorption kinetics, and effectiveness of adsorption were all factors investigated while evaluating the most promising materials that could be used as adsorbents.[10,25] Consequently, synthetic adsorbents, which can be made up of naturally occurring materials, have been thoroughly assessed and established to be exceptionally efficient and potentially valuable adsorbents to remove a wide range of soluble chemical contaminants.[4,25]

Recent studies have explored the utilization of advanced modified forms of clay minerals for the efficient and economical removal of organic and inorganic pollutants, demonstrating their remarkable effectiveness and environmental sustainability.[26,27] Kaolinite is classified as a variety of naturally occurring clay minerals, characterized by its composition, which is made up of hydrated aluminum silicate and the presence of 1 : 1 tetrahedron/octahedron stratified layers.[28–30] Despite the abundance and relatively inexpensive price of kaolinite when compared to various species of clay minerals that are supplied for commercial use, such as montmorillonite, there is a lack of comprehensive research on its potential to be used as a possible precursor for various environmental issues and industrial applications.[29,31,32] In comparison with bentonite, this was ascribed to the kaolinite's notably low surface area, restricted ion exchange opportunities, and weak adsorption capacity of soluble ions.[28,33] Consequently, several techniques, such as organic hybridization, peeling, exfoliating, scrolling, polymeric integration, and inorganic external decoration have all been used effectively to improve kaolinite's physical as well as chemical qualities.[28]

The chemical, biological, and physical characteristics of the manufactured materials are greatly affected by their morphological features. This is because the morphology plays a crucial role in determining the surface area, effectiveness of adsorption, and level of active site accessibility.[34] The utilization of nanomaterials that possess one-dimensional structures, such as nanorods and nanotubes, as well as two-dimensional geometrical forms, has been suggested for many potential uses because of their substantial surface area, superb dispersion qualities, and remarkable surface reactivity.[35–37] In the last few decades, there has been significant progress in the development of a sophisticated transformation process, including the separation of clay layers into distinct individual silicate sheets exhibiting two-dimensional geometries. The application of this method yielded favorable results in the generation of novel nanostructures composed of clay minerals, which exhibit notable attributes such as substantial biological performance, adsorption capacity, advanced oxidation activities, exterior reactive properties, anticancer qualities, surface area, and dispersion qualities.[29,31] Nevertheless, the focus of prior investigations has mostly been on assessing the implementation of this technique on montmorillonite, with little attention given to exfoliate kaolinite.[28,29] Moreover, it has been proposed that one-dimensional nanoparticles possess significant biological functionality, chemical reactivity, surface area, and catalytic abilities, making them extremely sophisticated nanomaterials that are suitable for many different kinds of industries.[36,37] Recently, it has been acknowledged that synthesized kaolinite nanoscrolls and nanotubes are novel and effective forms of adsorbents with exceptional surface area, a highly developed porous structure, and notable reactivity.[38] Clay nanotubes were developed through a straightforward procedure including the exfoliation of kaolinite sheets and, afterwards, a further process known as deduplication. This transformative step converts the exfoliated sheets into nanoscrolls, which are then subjected to ultrasonic vibrations and chemical-based expansion processes. The material obtained exhibits properties of semicrystallinity, a notable surface area, a highly organized porous structure, and remarkable adsorption capabilities.[33]

Regrettably, comprehensive investigations on the influence of kaolinite nanostructure morphology on its characteristics and efficacy as metal ion adsorbents have not yet been implemented to a suitable extent. Hence, the current work aims to examine the potential of synthetic kaolinite exfoliating nanosheets (EXK) and kaolinite nanotubes (KNTs) for effectively retaining cesium ions in comparison to raw kaolinite. The experimental investigations were conducted with a focus on the interfaces that exist across the applied adsorbent and the target soluble adsorbate. The attainment of this has been facilitated *via* the use of experimental observations and theoretical parameters generated according to advanced isotherm mathematical models developed through statistical physics concepts, which take into account both steric and energetic factors.

## 2 Experimental section

### 2.1. Materials

The kaolinite powders employed for the production of the exfoliated sheets (EXK) and nanotubes (KNTs) were acquired as

a purified sample from the Egyptian CMRDI (Central Metallurgical & Development Institute). Throughout the processes of exfoliation as well as scrolling, dimethyl sulfoxide (DMSO) with a purity of more than 99.5%, analytic grade cetyltrimethylammonium bromide (CTAB) with a purity of greater than 98%, and methanol with a purity of greater than 99.9% were delivered by Sigma-Aldrich; Egypt and used during the preparation procedures. The adsorption investigations implemented a $Cs^+$ standard solution with a concentration of 1000 mg $L^{-1}$.

### 2.2. Preparation of kaolinite exfoliated sheets (EXK) and nanotubes (KNTs)

The kaolinite-layers underwent exfoliation by a straightforward sonication support chemically expansion procedure. The kaolinite specimen underwent a pulverization process spanning 6 hours within a ball mill, resulting in the production of powder with particle sizes span a range of 20 to 100 μm. The pulverized kaolinite (15 g) had been then thoroughly mixed with 50 mL of dilute DMSO liquid (8 DMSO : 1 distilled water) for a duration of 5 hours by employing a typical magnetic stirring apparatus. The aforementioned procedure is crucial for the disruption of the prevailing hydrogen bonds that connect the stratified silicate sheet entities inside kaolinite. The kaolinite soaked in DMSO was later subjected to a series of washes incorporating methanol over duration of 20 minutes each. This process was repeated five times in order to eliminate the embedded DMSO groups and replaced by alcohol. As a result, an organophilic product known as methoxy kaolinite (Mth/K) has been developed. For a period of time, the Mth/K suspensions were homogenized with a pre-prepared CTAB mix (20 g CTAB + 50 mL of distilled water) for duration of 48 hours using a complex blending system consisting of a magnetic stirrer and an ultrasonic source (240 W). This process led to the development of exfoliated or disconnected kaolinite sheets (EXK). Then, the resulting EXK particles were subjected to a complete rinsing process using distilled water, followed by a gradual drying procedure at a temperature of 65 °C for duration of 12 hours. The resulting dried particles were then identified as EXK (Fig. 1).

After successfully completing the exfoliation steps, the system was further supplemented by the addition of 15 g of CTAB. Subsequently, the resultant mixture underwent an additional sonication step for a duration of 48 hours (240 W; 80%). This prolonged sonication duration aimed at promoting the complete expansion and rolling of the elastic silicate layers of kaolinite into nanotubes. Then, the final product was removed from the mix, subjected to a careful rinse using methanol alongside distilled water, and subsequently subjected to a drying process at a temperature of 65 °C for duration of 10 hours (Fig. 1).

### 2.3. Characterization techniques

The crystallization degrees and phase determination were assessed using a PANalytical-Empyrean X-ray diffractometer. This instrument has a measurement range spanning from 0 to 70 degrees. The chemical structural groups of EXK and KNTs, in comparison with kaolinite, were identified using a Fourier transform infrared spectrometer (FTIR8400S; Shimadzu) with a detection wavelength range of 400 to 4000 $cm^{-1}$. The morphologies of EXK and KNTs and their changes according to the kaolinite base morphology were examined during various transformation steps through the analysis of SEM photos. The photographs were acquired using a scanning electron microscopy (Gemini, Zeiss-Ultra 55) after applying thin coatings of gold to the surfaces of EXK and KNTs. Additionally, an assessment has been conducted on the internal characteristics of scrolled as well as exfoliated products *via* the analysis of their high-resolution transmission electron microscopy (HRTEM) photos. The photos were acquired using a JEOL-JEM2100 transmission electron microscope, operating at an acceleration voltage of 200 kV. The determination of surface areas was conducted using a Beckman Coulter SA3100 surface area analyzer. This was accomplished by evaluating the $N_2$ adsorption/desorption isotherms corresponding to the individual samples.

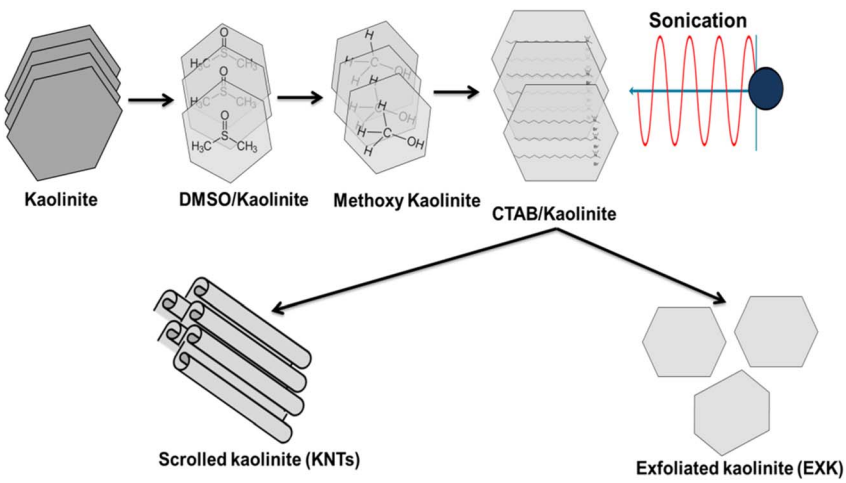


Fig. 1 Schematic diagram for the synthesis of exfoliated kaolinite (EXK) and kaolinite nanotubes (KNTs).

### 2.4. Adsorption studies

The batch examination involved conducting adsorption methods to remove cesium ions ($Cs^+$) using K, EXK, and KNTs. The study implemented commonly used experimental factors, including pH (ranging from 2 to 8), retention duration (ranging from 30 to 980 minutes), and $Cs^+$ concentration (ranging from 50 to 350 mg $L^{-1}$). Additionally, the testing temperature was varied within the range of 298 K to 313 K. Furthermore, the other primary testing variables were selected carefully and maintained at specific levels throughout the course of the investigation [tested volume: 100 mL; incorporated solid dosage: 0.4 g $L^{-1}$]. The experimental methodology was evaluated in triplicate, employing the average values of all measured concentrations as well as the derived calculations or observations. Following the completion of the equilibrium period for all the adsorption experiments, the solid particles of K, EXK, and KNTs have been separated out of $Cs^+$ solutions by the use of Whatman filter paper. The remaining $Cs^+$ concentration in the treated solutions had been measured by the use of inductively coupled plasma mass spectrometry (ICP-MS) provided by PerkinElmer. The $Cs^+$ standards employed for the measurements have been verified by the National Standard and Technology Institute (NIST), and the reference standards were obtained from Merck Company (Germany). The adsorption capacities ($Q_e$) of $Cs^+$ ions by K, EXK, and KNTs were determined in milligrams per gram (mg $g^{-1}$) using eqn (1). This calculation took into account the solutions, volume ($V$), the doses of K, EXK, and KNTs ($m$), the beginning concentration of $Cs^+$ ($C_o$), and the remaining concentration of $Cs^+$ ($C_e$).

$$Q_e(\text{mg g}^{-1}) = \frac{(C_o - C_e)V}{m} \quad (1)$$

### 2.5. Conventional and modern equilibrium modelling

The adsorption experiments have been simulated employing traditional kinetic, conventional isotherm, and advanced equilibrium modeling approaches, which were constructed using assumptions derived from statistical physics principles (Table S1†). Nonlinear fitting approaches were used to perform kinetic and conventional equilibrium modeling. This was completed considering the mathematical equations of the aforementioned models, and the outcomes in terms of the correlation coefficients ($R^2$) (eqn (2)) and chi-squared ($\chi^2$) (eqn (3)) were obtained as the main indicators of the fitting degrees. The determination of the appropriateness of the uptake processes' matching degrees with the assessed advanced equilibrium models has been accomplished by using the coefficient of correlation ($R^2$) plus the root mean square error (RMSE) (eqn (4)). The letters $m'$, $p$, $Q_{i,\text{cal}}$, and $Q_{i,\text{exp}}$ denote the experimental findings acquired, the parameters studied, the expected adsorption of $Cs^+$, and the verified capacity for $Cs^+$ adsorption, respectively.

$$R^2 = 1 - \frac{\sum (q_{e,\text{exp}} - q_{e,\text{cal}})^2}{\sum (q_{e,\text{exp}} - q_{e,\text{mean}})^2} \quad (2)$$

$$\chi^2 = \sum \frac{(q_{e,\text{exp}} - q_{e,\text{cal}})^2}{q_{e,\text{cal}}} \quad (3)$$

$$\text{RMSE} = \sqrt{\frac{\sum_{i=1}^{m} (Q_{i,\text{cal}} - Q_{i,\text{exp}})^2}{m' - p}} \quad (4)$$

## 3 Results & discussion

### 3.1. Characterization

The X-ray diffraction (XRD) patterns were employed to track the structural changes occurring during the conversion of kaolinite raw materials into single and exfoliated nano-kaolinite layers (EXK) and well-developed aluminosilicate nanotubes (KNTs) (Fig. 2). The triclinic, strongly crystalline kaolinite as the firstly applied crystalline phase has been distinguished by its distinct peaks at angles of about 12.3° (001), 20.8° (−110), 24.8° (002), and 26.6° (111) (Fig. 2A). The corresponding $d$-spacing value for these peaks has been determined to be 0.72 nm. Following the intercalation stage using DMSO, a notable reduction in the intensity of the typical diffraction peaks of kaolinite occurred, except for the peaks (001) and (002) that exhibited noticeable deviations (Fig. 2B). The diffraction chart produced following the sonication-accelerated exfoliating procedure with CTAB (EXK) showed a complete reduction in the intensity of all residual peaks, demonstrating that the reconstituted product was non-crystalline in nature (Fig. 2C). This observation provides evidence for the fact that kaolinite layers have been effectively separated into distinct, individual silicate layers characterized by their non-crystalline or sometimes semi-crystalline properties. The fabricated KNTs, exhibit a distinct X-ray diffraction (XRD) pattern characterized by a substantial decline in intensity for the standard peaks of kaolinite. Additionally, a new diminished peak has been noticed at a 2

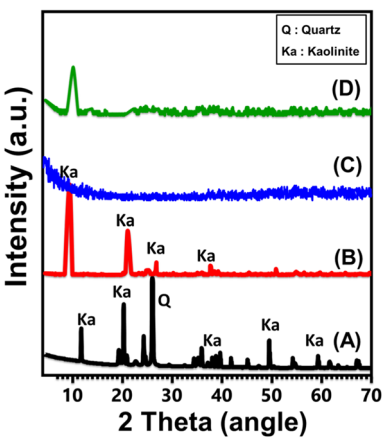


Fig. 2 XRD patterns of studied kaolinite precursor (A), DMSO modified kaolinite (B), synthetized EXK nanoparticles (C), and synthesized KNTs nanoparticles (D).

theta position of approximately 10.6°, which corresponds to the prominent peak associated with the (001) lattice planes of kaolinite nano-scrolls (Fig. 2D).

Regarding the morphological alterations recognized over the different synthesizing procedures, the original kaolinite granules exhibited a stacked arrangement of pseudo-hexagonal flakes or plate-like particles, as evident from both the HRTEM and the SEM images (Fig. S1†). The analyzed HRTEM images of the exfoliating products indicate substantial scraping and splitting of the kaolinite, forming individual layers (Fig. 3A). Further inspection of the examined photos displayed the existence of the distinct kaolinite silicate layers that were separating, exhibiting a noteworthy retention of the pseudo-hexagonal shape. However, the borders of these divided layers seemed to be smoother compared to the original kaolinite flakes (Fig. 3B). Certain samples exhibit milder shades of gray in comparison to the predominant gray shade that dominates the kaolinite sheets, indicating a lack of ordering in the fundamental silicate units comprising kaolinite (Fig. 3C). The effective fabrication of the KNTs was further confirmed by the examination of SEM alongside HRTEM images (Fig. 3D–F). The single flakes of the kaolinite material sustained a notable conversion, resulting in the development of folded or scrolled nanostructures exhibiting tabulated morphologies (Fig. 3D). The investigation revealed that the rolling particulates had cylindrical shapes characterized by hollow interior properties, with internal widths spanning from 2 until 20 nm (Fig. 3E and F). The synthetic KNTs' assessed dimension ranged from approximately 50 nm upwards to nearly 600 nm, while their exterior diameter was found to be fluctuating within the range of 10 until 50 nm. The surface area of kaolinite undergoes significant improvement through the morphological modifications performed. Specifically, the surface area of unprocessed kaolinite, initially measured at 10 $m^2$ $g^{-1}$, increases to about 80.2 $m^2$ $g^{-1}$ and nearly 105 $m^2$ $g^{-1}$ afterwards undergoing the exfoliating (EXK) and rolling procedures (KNTs), respectively.

The FT-IR spectra were used to evaluate the effect of the geometrical transformation process from kaolinite compacted flakes into EXK or KNTs on the silicate structure, specifically in terms of their chemical functionalities. The infrared spectrum of kaolinite exhibits distinct bands corresponding to the distinguished functional groups present in its aluminosilicate structure (Fig. 4). These include Si–O vibrations at 787 and 456 $cm^{-1}$, Si–O–Al vibrations at 526 and 680 $cm^{-1}$, Si–O–Si vibrations at 1020 $cm^{-1}$, Al–OH vibrations at 912 and 3500 $cm^{-1}$, O–H vibrations at 1641 $cm^{-1}$, and Si–OH vibrations at 3689 $cm^{-1}$ (ref. 29 and 39) (Fig. 4A). The spectrum of EXK exhibit identical absorption bands that have been reported in unprocessed kaolinite raw mineral, except considerable variations in the positions of them, reductions in intensity, and a splitting of identifiable bands at roughly 900 to 1000 $cm^{-1}$ (Fig. 4B). This denotes the successful dissociation of the aluminosilicate layers that comprise kaolinite, resulting in the formation of monolayer layers or individual nanosheets. It is also expected that this process would cause distortions within the octahedron as well as tetrahedron structural units.[33,40] Similar findings have been documented throughout the evaluation of the synthetically generated KNTs' FT-IR spectrum particulates (Fig. 4C). The relative assignments of the matching bands of the aluminosilicate framework exhibited notable deviations when compared with their

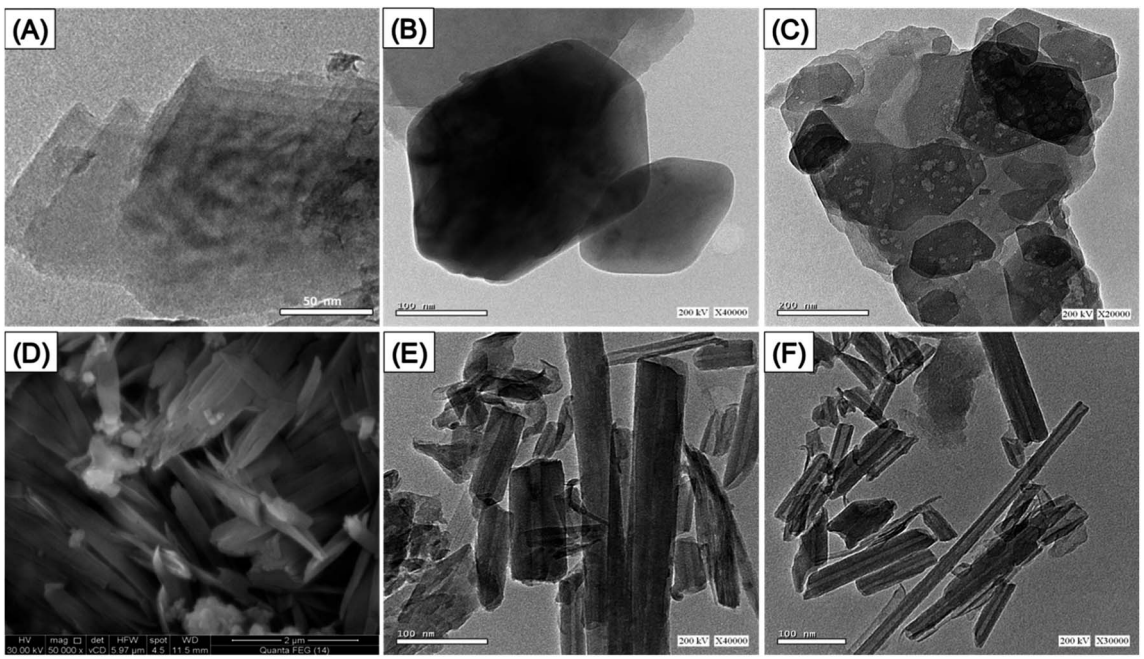


Fig. 3 HRTEM images of the synthetized EXK nanoparticles (A–C), SEM of synthesized KNTs (D), and HRTEM images of the synthesized KNTs nanoparticles (E and F).

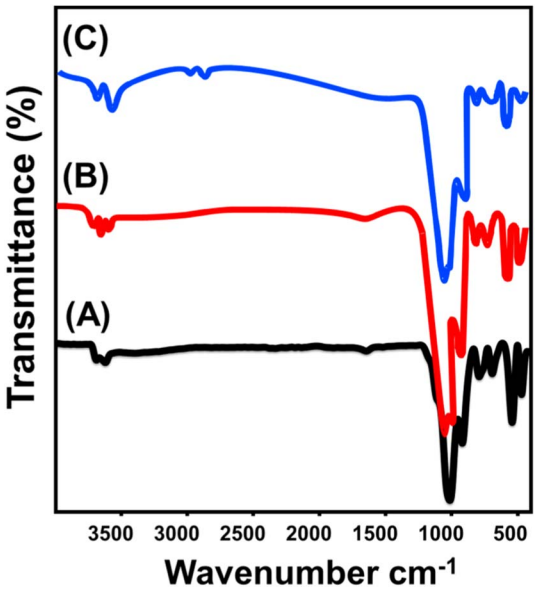


Fig. 4 FT-IR spectra of studied kaolinite precursor (A), synthetized EXK nanoparticles (B), and synthesized KNTs nanoparticles (C).

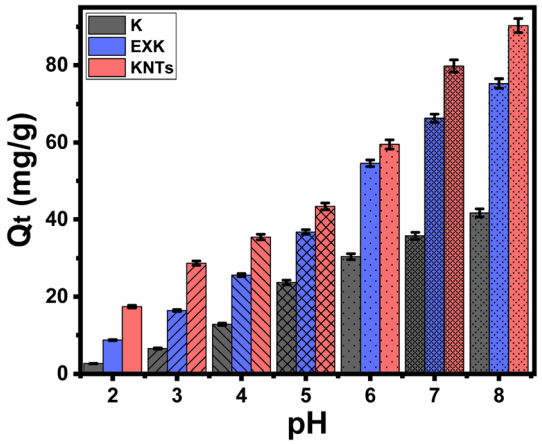


Fig. 5 The influence of the pH values on the retention of $Cs^+$ ions by KA, EXK, and KNTs.

equivalent sites for kaolinite. Furthermore, this observation indicates the transformation caused by the exfoliating and scrolling alterations on the fundamental octahedron as well as tetrahedron units. Additionally, it highlights the influence of the freshly developed hydrogen bonds that link the employed organic compounds and the hydroxyl-bearing functionalities of kaolinite (Fig. 4C).[33]

### 3.2. Adsorption studies

**3.2.1. Effect of pH.** The impact of pH levels ranging from 2 to 8 on the ability of $Cs^+$ to be adsorbed using KA, EXK, and KNTs as particularly successful adsorbents has been investigated. All the laboratory tests stated above had been successfully conducted by meticulously controlling all the major variables at their designated values, including the $Cs^+$ concentration of 100 mg $L^{-1}$, solid dose of 0.4 g $L^{-1}$, volume of 100 mL, temperature of 25 °C, and duration of 120 minutes. The observed $Cs^+$ retention capacities employing KA, EXK, and KNTs exhibit significant enhancements as the pH of the examined contaminated solutions raises from pH 2 (2.6 mg $g^{-1}$ (KA), 8.7 mg $g^{-1}$ (EXK), and 17.4 mg $g^{-1}$ (KNTs)) to pH 8 (41.7 mg $g^{-1}$ (KA), 75.3 mg $g^{-1}$ (EXK), and 90.3 mg $g^{-1}$ (KNTs)) (Fig. 5). Consequently, those types of materials can serve as highly successful adsorbents in practical purification processes in accordance with the pH range of 6 to 9 that the US EPA recommends for the remediation of industrial wastewater.[41] The behaviors that were reported exhibit a strong correlation with the notable impact of pH on both the ionizing characteristics of the $Cs^+$ ions as well as the prevailing charges found across the KA, EXK, and KNTs' exterior surfaces.[42] As alkaline extents of $Cs^+$ solutions increased, the chemically reactive structural groups of KA, EXK, and KNTs continued to deprotonate, resulting in their exterior surfaces becoming completely saturated with negative electrostatic charges.[43] The negatively charged outside surfaces of KA, EXK, and KNTs serve as vital centers mediating the electrostatic attractions of $Cs^+$ with its positive charge.[3] The zero points of charge's pH ($pH_{(ZPC)}$) values are 7.3 for KA, 6.2 for EXK, and 5.8 for KNTs, which are consistent with prior findings about the dominance of negative charges beyond these values.

### 3.2.2. Kinetic studies

*3.2.2.1. Effect of contact time.* Throughout a time range of 30 minutes to 980 minutes, the laboratory-measured impact of $Cs^+$ uptake periods on the KA, EXK, and KNTs' experimentally verified qualities was investigated. This was attained subsequent to the adjustment of other influential variables to specific values [$Cs^+$ level: 100 mg $L^{-1}$; pH: 8; volumes: 100 mL; temperature: 25 °C; solid material dosage: 0.4 g $L^{-1}$]. The efficiency of KA, EXK, and KNTs in adsorbing $Cs^+$ is evident from the significant increase in observable uptake rates alongside the calculated amounts of retained $Cs^+$ in mg $g^{-1}$. Additionally, the time frame of the tests has a controlling effect on these observed increases (Fig. 6A). The observed enhanced influence of the $Cs^+$ retention behaviors utilizing (KA), (EXK), and (KNTs) may be readily discerned for a duration of up to 240 minutes (KA) and 500 minutes (EXK and KNTs). After the specified contact time, there were no apparent shifts or increases in the rates of $Cs^+$ retention or the amounts of $Cs^+$ immobilized (Fig. 6A). This suggests that the system reached a level of stabilization at 240 minutes (KA) and 500 minutes (EXK and KNTs) identified as adsorption equilibrium (Fig. 6A). It can be observed that the $Cs^+$ equilibrium retention limits of the KA, EXK, and KNTs particulates were 52.4 mg $g^{-1}$ (KA), 109.6 mg $g^{-1}$ (EXK), and 131.8 mg $g^{-1}$ (KNTs) (Fig. 6A). The initial stages of the experiments conducted demonstrated that the presence of abundant free and functionally reactive groups or retention receptors on the outermost layers of KA, EXK, and KNTs has led to noticeable increases in both the rate of $Cs^+$ uptake and the amounts of $Cs^+$ adsorbed.[44] The extended retention of $Cs^+$ onto the receptors of KA, EXK, and KNTs leads to their occupation and depletion, resulting in

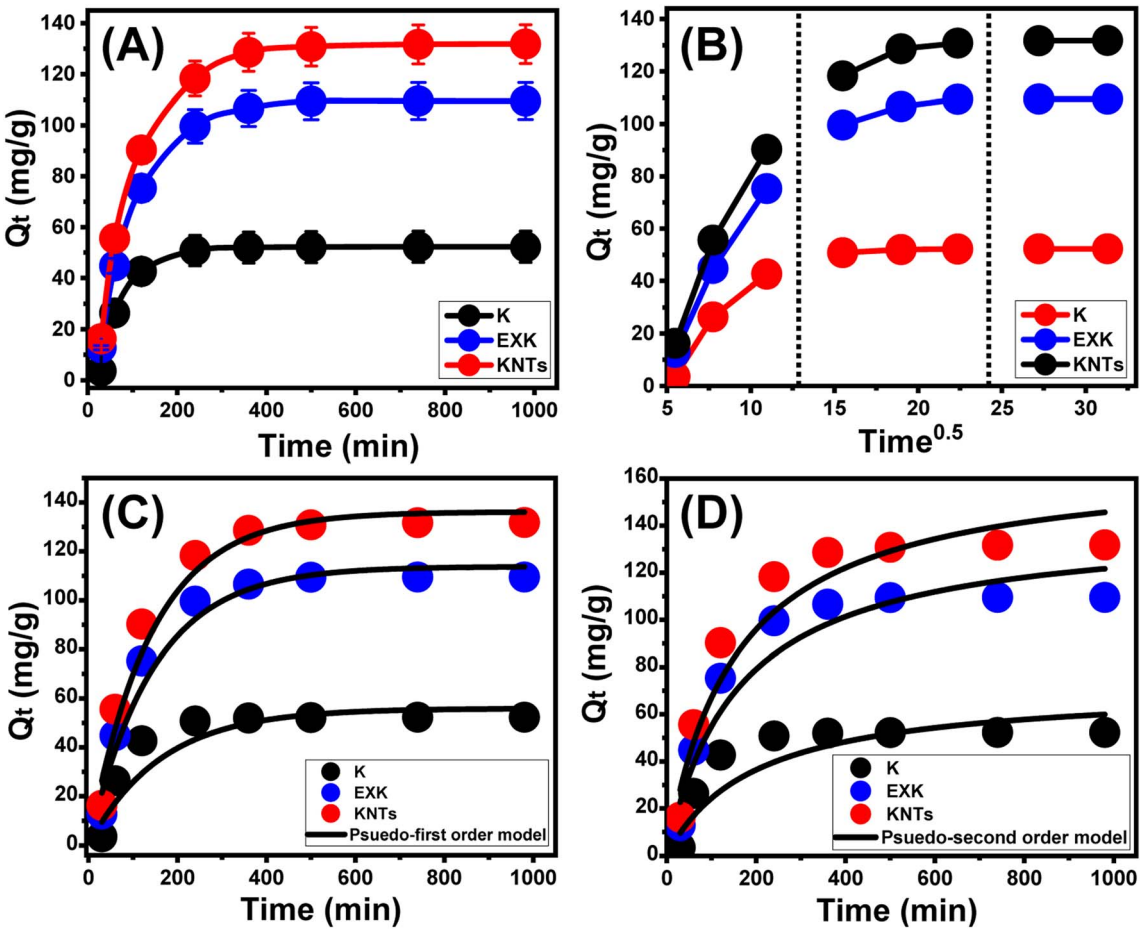


Fig. 6 The influence of contact time on the retention of $Cs^+$ ions by KA, EXK, and KNTs (A), intra-particle diffusion curves (B), pseudo-first order kinetic model (C), and pseudo-second order kinetic model (D) [$Cs^+$ level: 100 mg $L^{-1}$; pH: 8; volumes: 100 mL; temperature: 25 °C; dosage: 0.4 g $L^{-1}$; time: 30–980 min].

a significant decrease in their accessibility as the duration of the tests is prolonged. Consequently, after a designated period of time, the uptake rates of the $Cs^+$ suffered a significant reduction, while the retention characteristics of KA, EXK, and KNTs remained the same or showed disregarded enhancement. Upon the complete occupation of receptors or free sites of reaction by $Cs^+$, the equilibrium conditions of KA, EXK, and KNTs have been established.[2]

*3.2.2.2. Intra-particle diffusion behavior.* The $Cs^+$ uptake behaviors by KA, EXK, and KNTs are characterized by intra-particle diffusion curves, which exhibit three distinctive segments with varying slopes (Fig. 6B). The accomplished curves in the present investigation exhibit no noticeable crossings with the starting points, suggesting that many pathways involved in $Cs^+$ adsorption are present in conjunction with $Cs^+$ diffusion mechanisms.[42,45] The operational process may encompass the following key steps: (A) the capture of $Cs^+$ *via* the receptors dispersed across the external surfaces of KA, EXK, and KNTs (boundary), (B) intra-particle diffusion, and (C) the operational reaction involving the phase of saturation as well as stability states.[46] The initial phase of this investigation indicates that the exterior adsorption reactions of $Cs^+$ were the most controlling pathways implemented during the experimentation (Fig. 6B). The effectiveness of the $Cs^+$ retention reaction throughout this phase is dependent on the overall quantities of surficial unoccupied receptors of KA, EXK, and KNTs.[47] The detection of newly developed phases was facilitated by extending the duration, demonstrating the efficacy of several supplementary mechanisms referred to as layered adsorption procedures (Fig. 6B).[3,46] These additional processes also encompass the impact of $Cs^+$ diffusion operations. Ultimately, it has been noted that the last three phases exhibit predominance when KA, EXK, and KNTs attain a condition of equilibrium with $Cs^+$ adsorption (Fig. 6B). This observation indicates that all of the $Cs^+$ ions that were successfully retained have occupied all of the available binding receptors.[2,4] In the meantime, the removal of $Cs^+$ is influenced by multiple factors, potentially including molecular interactions and interionic attraction pathways.[43]

*3.2.2.3. Kinetic modeling.* The kinetic features of the $Cs^+$ retention activities *via* KA, EXK, and KNTs were elucidated using the conventional kinetic assumptions of both the pseudo-first order (P.F.) along with pseudo-second order (P.S.) numerical models. The degree of concordance between the $Cs^+$ retention activities and the kinetic hypotheses of each of the two

models was evaluated using established nonlinear fitting parameters, as indicated by the respective equations and established by both the correlation coefficient ($R^2$) and the chi-squared ($\chi^2$) statistic (Table 1; Fig. 6C and D). The levels of $R^2$ accomplished, together with $\chi^2$, indicate that the kinetic behavior and concepts of the P.F. model provide a better fit for the adsorption activities of $Cs^+$ by KA, EXK, and KNTs compared to the evaluated P.S. model. The findings from the experiments conducted on KA, EXK, and KNTs during their equilibrium conditions (52.3 mg $g^{-1}$ (KA), 109.5 mg $g^{-1}$ (EXK), and 131.8 mg $g^{-1}$ (KNTs)) were found to be remarkably consistent with the values obtained through mathematical computations from the model (55.9 mg $g^{-1}$ (KA), 113.7 mg $g^{-1}$ (EXK), and 136.1 mg $g^{-1}$ (KNTs)). This agreement further supports the prior kinetic observations (Table 1). Based on the fundamental principles of the P.F. hypothesis, it is suggested that the primary factors influencing the $Cs^+$ sequestration involving KA, EXK, and KNTs are physical pathways, including the forces of van der Waals along with attraction to electrostatic charges.[48,49] Despite the P.F. model's equation for removing $Cs^+$ *via* KA, EXK, and KNTs being more compatible than the depicted formula for the P.S. concept, the observed retention characteristics nevertheless demonstrate significant concordance with the P.S. kinetics. Consequently, prior research has indicated that several commonly observed weak chemical phenomena, including chemical complexing, hydrophobic interactions, hydrogen bonding, and electron-based sharing, are expected to either facilitate or have minor impacts on the elimination of $Cs^+$ by KA, EXK, and KNTs.[42,48] After a chemically binding $Cs^+$ layer, a physically absorbed $Cs^+$ layer was formed, utilizing the earlier layer as a base.[50]

Table 1 The mathematical parameters of the studied kinetic models

| Material | Model | Parameters | Values |
|---|---|---|---|
| K | Pseudo-first-order | $K_1$ ($min^{-1}$) | 0.0061 |
| | | $Q_{e(cal)}$ (mg $g^{-1}$) | 55.9 |
| | | $R^2$ | 0.90 |
| | | $\chi^2$ | 3.08 |
| | Pseudo-second-order | $K_2$ (mg $g^{-1}$ $min^{-1}$) | $7.16 \times 10^{-5}$ |
| | | $Q_{e(cal)}$ (mg $g^{-1}$) | 71.8 |
| | | $R^2$ | 0.85 |
| | | $\chi^2$ | 3.85 |
| EXK | Pseudo-first-order | $K_1$ ($min^{-1}$) | 0.0069 |
| | | $Q_{e(cal)}$ (mg $g^{-1}$) | 113.7 |
| | | $R^2$ | 0.96 |
| | | $\chi^2$ | 1.5 |
| | Pseudo-second-order | $K_2$ (mg $g^{-1}$ $min^{-1}$) | $4.5 \times 10^{-5}$ |
| | | $Q_{e(cal)}$ (mg $g^{-1}$) | 141.2 |
| | | $R^2$ | 0.94 |
| | | $\chi^2$ | 2.58 |
| KNTs | Pseudo-first-order | $K_1$ ($min^{-1}$) | 0.0071 |
| | | $Q_{e(cal)}$ (mg $g^{-1}$) | 136.1 |
| | | $R^2$ | 0.96 |
| | | $\chi^2$ | 1.59 |
| | Pseudo-second-order | $K_2$ (mg $g^{-1}$ $min^{-1}$) | $3.96 \times 10^{-5}$ |
| | | $Q_{e(cal)}$ (mg $g^{-1}$) | 167.9 |
| | | $R^2$ | 0.93 |
| | | $\chi^2$ | 2.79 |

### 3.2.3. Equilibrium studies

*3.2.3.1. Effect of $Cs^+$ concentrations.* The effect of the initial $Cs^+$ concentrations has been investigated to be able to ascertain the optimal capacities of KA, EXK, and KNTs as well as their states of equilibrium across the experimentally established limits ranging from 50 to 350 mg $L^{-1}$. The rest of the retention variables have been selected to be at predetermined levels [solid quantity: 0.4 g $L^{-1}$; time: 24 hours; treated volume: about 100 mL; temperature: from 298 K to 313 K]. The total amounts of $Cs^+$ retained by KA, EXK, and KNTs exhibited a notable rise at increasing concentrations of $Cs^+$ (Fig. 7A–C). The strengthened levels of $Cs^+$ ions inside a specific volume resulted in a discernible enhancement in their transportation, diffusion, and driving forces, thereby facilitating interactions along with collision opportunities with the largest number of available free and functioning receptors positioned across the KA, EXK, and KNTs' exterior surfaces. This led to a significant improvement in the efficiency of the $Cs^+$ adsorption reactions performed by KA, EXK, and KNTs.[51] The measurable quantities of $Cs^+$ absorbed exhibit an increase relative to the raised initial concentration, up to certain levels. Subsequently, a rise in the initial level of $Cs^+$ has no noticeable impact on the quantities of ions that KA, EXK, and KNTs retain, hence differentiating their equilibrium phases and determining the actual maximum $CS^+$ adsorption potential. After 250 mg $L^{-1}$, the equilibration settings in the existence of KA correspond to adsorption values of 72.7 mg $g^{-1}$ (298 K), 60.8 mg $g^{-1}$ (308 K), and 49.2 mg $g^{-1}$ (313 K) (Fig. 7A). The equilibrium capacities obtained for EXK after testing 250 mg $L^{-1}$ of $Cs^+$ are 198.4 mg $g^{-1}$ at 298 K, 164.3 mg $g^{-1}$ at 308 K, and 126.6 mg $g^{-1}$ at 313 K (Fig. 7B). The corresponding $Cs^+$ concentration of equilibrium for KNTs is estimated to be 250 mg $L^{-1}$, with related capacities of 247.5 mg $g^{-1}$ at 298 K, 208.6 mg $g^{-1}$ at 308 K, and 171.8 mg $g^{-1}$ at 313 K (Fig. 7C). The remarkable efficiency of EXK and KNTs in eliminating $Cs^+$ in comparison to KA particulates may be ascribed to both the aluminosilicate layers' reactivity character and the significant surface area rise, which exhibit semi-crystalline characteristics and have a high number of exposed chemically active sites, particularly the siloxane groups. The reduction in adsorption of $Cs^+$ by K, EXK, and KNTs as a function of temperature suggests that the processes are exothermic.

**3.2.4. Giles's classification.** The $Cs^+$ isotherm curves using KA, EXK, and KNTs were categorized according to the guidelines established by Giles' classification. The investigation established that these curves exhibited an L-type state of equilibrium (Fig. 7A–C). The L-type's equilibrium characteristics show the significant influence of the intermolecular attracting forces operating whenever KA, EXK, and KNTs adsorb $Cs^+$. These effects are further amplified by the strong $Cs^+$ ion reaction with the chemically reactive frameworks of KA, EXK, and KNTs.[52] On the basis of L-type isotherm specifications, it was also possible to forecast a full generation of retained $Cs^+$ monolayers across the exterior interfaces of KA, EXK, and KNTs particulates.[53] Moreover, the observed isothermal pattern indicates the production of KA, EXK, and KNTs particles with various and massive functional and unbound uptake receptors. These

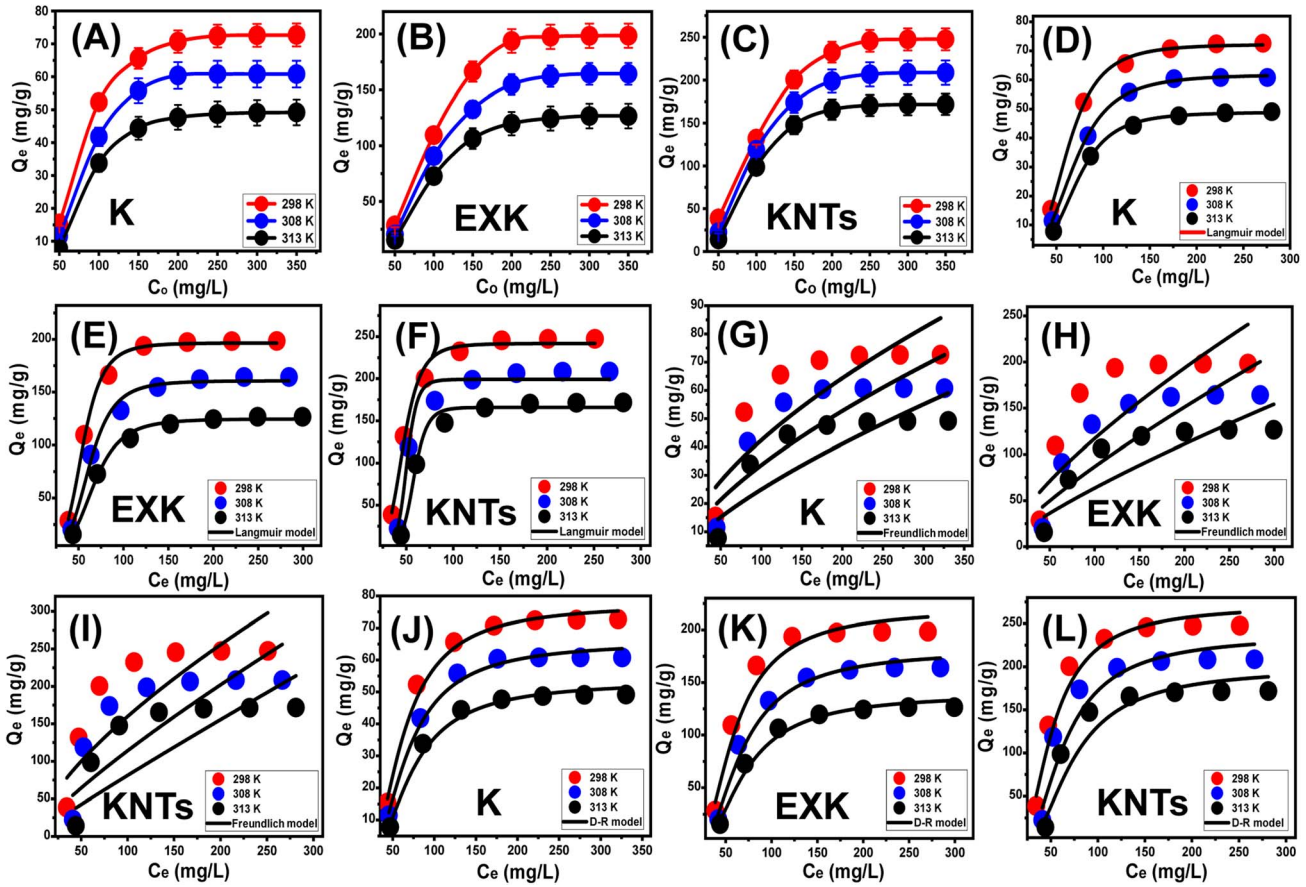


Fig. 7 The influence of initial $Cs^+$ concentrations on the determined retention capacities (KA (A), EXK (B), and KNTs (C)), non-linear fitting of the $Cs^+$ retention with conventional Langmuir model (KA (D), EXK (E), and KNTs (F)), Freundlich model (KA (G), EXK (H), and KNTs (I)), and D–R model (KA (J), EXK (K), and KNTs (L)).

receptors demonstrate significant selectivity towards the $Cs^+$ ions across the entire adsorption process, especially when the initial concentrations are low.

**3.2.5. Classic isotherm models.** The present study examines the equilibrium remarks of $Cs^+$ retention by KA, EXK, and KNTs particles employing the isotherm perspectives of Langmuir in addition to Freundlich along with Dubinin–Radushkevich (D–R). The level of consistency with the isotherm hypotheses of each of the specified models and the experimentally determined $Cs^+$ retention activities was assessed based on the non-linear fit degrees implementing the respective equations of the different models. This evaluation was designed according to the correlation coefficient ($R^2$) and the chi-squared ($\chi^2$) values (Table 2 and Fig. 7D–L). The results obtained from the analysis of $R^2$ and $\chi^2$ indicate that the $Cs^+$ retention activities displayed by KA, EXK, and KNTs particles align more closely with the fundamentals of the Langmuir isotherm model compared to the underlying hypotheses of the Freundlich model (Table 2 and Fig. 7D–L). The Langmuir isotherm describes the uniform adsorption of $Cs^+$ ions on the unoccupied and activated binding sites of KA, EXK, and KNTs particles in a monolayer format.[48,49] Furthermore, it has been demonstrated that the $Cs^+$ retention characteristics of KA, EXK, and KNTs particles exhibit RL values below 1, indicating the favorable characteristics of these reactions.[4,47] The hypothesized maximum adsorption capacity ($Q_{max}$) of $Cs^+$ by KA at different temperatures is as follows: 73.3 mg $g^{-1}$ (298 K), 62.8 mg $g^{-1}$ (308 K), and 49.9 mg $g^{-1}$ (313 K). The computing values from the model using EXK are 200.5 mg $g^{-1}$ (298 K), 168.8 mg $g^{-1}$ (308 K), and 130.6 mg $g^{-1}$ (313 K). The theoretical maximal capacities for adsorption of $Cs^+$ ($Q_{max}$) by KNTs at different temperatures are as follows: 251.9 mg $g^{-1}$ at 298 K, 219.8 mg $g^{-1}$ at 303 K, and 186.1 mg $g^{-1}$ at 313 K (Table 2).

The D–R model's postulated equilibrium elements (Fig. 7J–L) provide a comprehensive understanding of the energy variations displayed by KA, EXK, and KNTs particles throughout the process of $Cs^+$ retention, irrespective of the system's homogeneity or heterogeneity.[54] The Gaussian energy ($E$) is a quantitative measure obtained from the D–R assessment outcomes, plays a crucial role in identifying the specific $Cs^+$ uptake pathways (chemical or physical). According to previous studies conducted by Sayed *et al.*,[4] and Dawodu *et al.*,[54] adsorption operations characterized by $E$ values below 8 kJ $mol^{-1}$, between 8 and 16 kJ $mol^{-1}$, and above 16 kJ $mol^{-1}$ suggest the presence of mostly physical interactions, relatively weak chemical interactions or a combination of complicated physical and chemical

Table 2 The theoretical constraints of the traditional isotherm models under study

| | | | 298 K | 308 K | 313 K |
|---|---|---|---|---|---|
| KA | Langmuir model | $Q_{max}$ (mg g$^{-1}$) | 73.32 | 62.88 | 49.9 |
| | | $b$ (L mg$^{-1}$) | $1.89 \times 10^{-7}$ | $3.2 \times 10^{-7}$ | $4.4 \times 10^{-8}$ |
| | | $R^2$ | 0.99 | 0.99 | 0.99 |
| | | $\chi^2$ | 0.021 | 0.006 | 0.005 |
| | Freundlich model | $1/n$ | 0.6 | 0.65 | 0.72 |
| | | $k_F$ (mg g$^{-1}$) | 2.6 | 1.64 | 0.89 |
| | | $R^2$ | 0.79 | 0.8 | 0.8 |
| | | $\chi^2$ | 4.2 | 3.9 | 3.6 |
| | D–R model | $\beta$ (mol$^2$ kJ$^{-2}$) | 0.0067 | 0.0078 | 0.0082 |
| | | $Q_m$ (mg g$^{-1}$) | 77.5 | 65.6 | 53.2 |
| | | $R^2$ | 0.993 | 0.994 | 0.993 |
| | | $\chi^2$ | 0.12 | 0.10 | 0.11 |
| | | $E$ (kJ mol$^{-1}$) | 8.63 | 8.006 | 7.8 |
| EXK | Langmuir model | $Q_{max}$ (mg g$^{-1}$) | 200.5 | 168.8 | 130.6 |
| | | $b$ (L mg$^{-1}$) | $2.34 \times 10^{-9}$ | $3.9 \times 10^{-9}$ | $6.7 \times 10^{-9}$ |
| | | $R^2$ | 0.99 | 0.99 | 0.99 |
| | | $\chi^2$ | 0.188 | 0.379 | 0.109 |
| | Freundlich model | $1/n$ | 0.72 | 0.46 | 0.81 |
| | | $k_F$ (mg g$^{-1}$) | 4.1 | 2.15 | 1.5 |
| | | $R^2$ | 0.75 | 0.79 | 0.79 |
| | | $\chi^2$ | 9.19 | 5.05 | 2.34 |
| | D–R model | $\beta$ (mol$^2$ kJ$^{-2}$) | 0.0031 | 0.0037 | 0.0046 |
| | | $Q_m$ (mg g$^{-1}$) | 225.3 | 180.9 | 138.9 |
| | | $R^2$ | 0.97 | 0.98 | 0.99 |
| | | $\chi^2$ | 1.6 | 0.9 | 0.5 |
| | | $E$ (kJ mol$^{-1}$) | 12.7 | 11.6 | 10.42 |
| KNTs | Langmuir model | $Q_{max}$ (mg g$^{-1}$) | 251.9 | 219.8 | 186.1 |
| | | $b$ (L mg$^{-1}$) | $2.45 \times 10^{-9}$ | $5.4 \times 10^{-9}$ | $7.8 \times 10^{-9}$ |
| | | $R^2$ | 0.99 | 0.98 | 0.99 |
| | | $\chi^2$ | 0.528 | 1.048 | 0.508 |
| | Freundlich model | $1/n$ | 0.66 | 0.61 | 0.5 |
| | | $k_F$ (mg g$^{-1}$) | 378.7 | 308.8 | 231.6 |
| | | $R^2$ | 0.998 | 0.995 | 0.998 |
| | | $\chi^2$ | 0.29 | 0.47 | 0.31 |
| | D–R model | $\beta$ (mol$^2$ kJ$^{-2}$) | 0.0038 | 0.0044 | 0.0051 |
| | | $Q_m$ (mg g$^{-1}$) | 271.2 | 236.5 | 198.6 |
| | | $R^2$ | 0.97 | 0.93 | 0.94 |
| | | $\chi^2$ | 2.2 | 6.3 | 5.5 |
| | | $E$ (kJ mol$^{-1}$) | 11.4 | 10.6 | 9.9 |

interactions, and strong chemical mechanisms, respectively. The calculated values for the $E$ factor related to $Cs^+$ retention activities by KA, EXK, and KNTs align with the supposed energies proposed for the cooperative mechanisms of weak chemical and physical processes (8 to 16 kJ mol$^{-1}$), as supported by the mathematical findings obtained from the kinetic investigations (Table 2).

**3.2.6. Advanced isotherm studies.** Depending upon the basic tenets of the statistical physics assumption, most recent developments in equilibrium models have the potential to provide significant insights into the distinct characteristics of adsorption processes, particularly in relation to the interfaces between adsorbents and adsorbates, as well as the external properties of heterogeneous solid adsorbents. The statistical aspects developed using these equations, including steric and energy variables, may be implemented to clarify the underlying pathways. The steric aspects were three key parameters: the total amount of $Cs^+$ ions that exist at each site ($n_{(Cs^+)}$), the total number of sites filled with $Cs^+$ across the exteriors of KA, EXK, and KNTs ($N_{m(Cs^+)}$), and the greatest ability of KA, EXK, and KNTs to absorb $Cs^+$ after fully saturated ($Q_{sat(Cs^+)}$). The factors combined with energetic properties included internal energy ($E_{int}$), free enthalpy ($G$), entropy ($S_a$), and $Cs^+$ elimination energy ($E$). The statistical model that has been developed to analyze the $Cs^+$ retention behaviors was assessed utilizing non-linear fits with the relevant equations associated with these models. The aforementioned task was accomplished by using multivariable nonlinear regression analysis in conjunction with the Levenberg–Marquardt iterative methodology. Based on the observed levels of fitness, a monolayer model with a single energetic site (M1) has been employed to analyze and describe the adsorption mechanisms of $Cs^+$ by KA, EXK, and KNTs. This analysis as illustrated in Fig. 8A–C and Table 3.

**3.2.7. Steric studies**

*3.2.7.1. Quantity of adsorbed $Cs^+$ ($n_{(Cs^+)}$) at single site.* The numerical findings pertaining to the $n_{(Cs^+)}$ factor strongly suggest the arrangement (vertical or horizontal) of the cesium ions that have been captured on the surfaces of KA, EXK, and

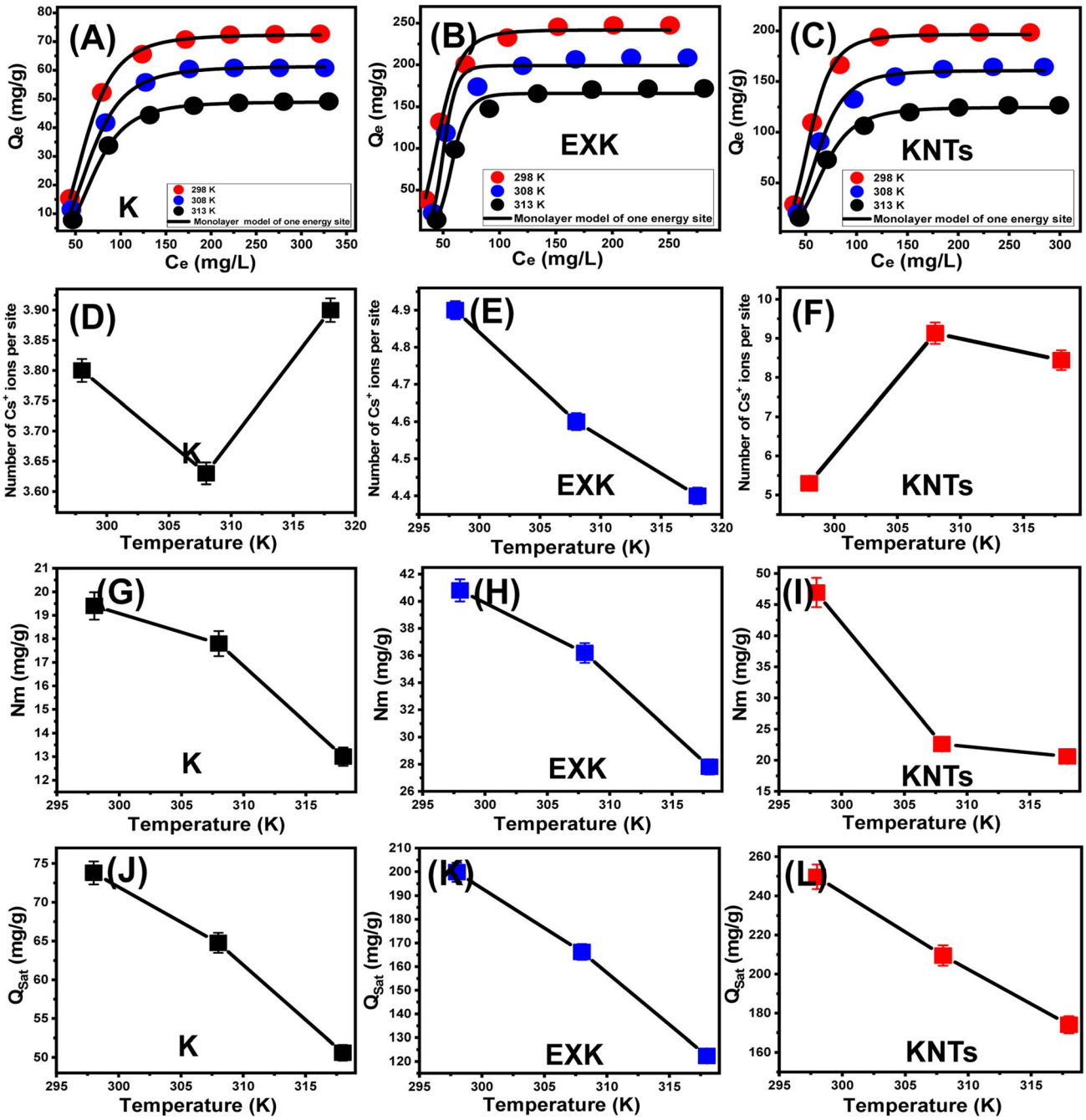


Fig. 8 Fitting of the $Cs^+$ retention with monolayer model with a single energetic site (KA (A), EXK (B), and KNTs (C)), variations in the quantity of $Cs^+$ ions trapped at each site (KA (D), EXK (E), and KNTs (F)), variations in the amount of filled active sites following the capture of $Cs^+$ (KA (G), EXK (H), and KNTs (I)), and changes in the $Cs^+$ saturation uptake capacities (KA (J), EXK (K), and KNTs (L)).

KNTs. These results possess additional implications for establishing the mechanistic procedures involved, specifically the distinction between multi-docking and multi-ionic. In systems affected by multi-anchorage or multi-docking actions, one $Cs^+$ ion is retained by numerous adsorption sites within horizontal patterns. For processes with values exceeding one, a number of $Cs^+$ ions may be captured through just a single binding site within non-parallel alongside vertical positions, and these retention behaviors are primarily triggered by multi-ionic mechanistic.[4,55] The determined values of $n_{(Cs^+)}$ for KA ($n_{(Cs^+)}$ = 3.6–3.9), EXK ($n_{(Cs^+)}$ = 4.4–4.9), and KNTs ($n_{(Cs^+)}$ = 5.15–9.5) exhibit values greater than 1 (Table 3 and Fig. 8D–F). Consequently, the $Cs^+$ ions were adsorbed according to multi-ionic mechanisms, wherein each adsorbent absorption site had the capacity to accommodate up to four ions by KA, five ions using EXK, and ten ions using KNTs that were distributed in a non-parallel vertical orientation. These findings also verify the exceptional impact that the morphological alterations have on

Table 3 The computational constraints of the advanced isotherm model under consideration

| | | 298 K | 308 K | 313 K |
|---|---|---|---|---|
| KA | $R^2$ | 0.9993 | 0.998 | 0.997 |
| | $\chi^2$ | 0.016 | 0.0037 | 0.0048 |
| | $n$ | 3.8 | 3.63 | 3.9 |
| | $N_m$ (mg g$^{-1}$) | 19.4 | 17.8 | 13.0 |
| | $Q_{sat}$ (mg g$^{-1}$) | 73.78 | 64.7 | 50.6 |
| | $C_{1/2}$ (mg L$^{-1}$) | 62.1 | 67.7 | 71.2 |
| | $\Delta E$ (kJ mol$^{-1}$) | −8.4 | −8.3 | −8.5 |
| EXK | $R^2$ | 0.998 | 0.995 | 0.998 |
| | $\chi^2$ | 0.18 | 0.37 | 0.1 |
| | $n$ | 4.9 | 4.6 | 4.4 |
| | $N_m$ (mg g$^{-1}$) | 40.8 | 36.19 | 27.8 |
| | $Q_{sat}$ (mg g$^{-1}$) | 199.8 | 166.2 | 122.3 |
| | $C_{1/2}$ (mg L$^{-1}$) | 54.6 | 62.1 | 66.9 |
| | $\Delta E$ (kJ mol$^{-1}$) | −8.7 | −8.5 | −8.6 |
| KNTs | $R^2$ | 0.995 | 0.991 | 0.995 |
| | $\chi^2$ | 0.5 | 1.04 | 0.5 |
| | $n$ | 5.3 | 9.13 | 8.44 |
| | $N_m$ (mg g$^{-1}$) | 46.94 | 22.6 | 20.6 |
| | $Q_{sat}$ (mg g$^{-1}$) | 249.7 | 209.5 | 174.05 |
| | $C_{1/2}$ (mg L$^{-1}$) | 46.9 | 50.6 | 58.2 |
| | $\Delta E$ (kJ mol$^{-1}$) | −9.12 | −9.08 | −9.02 |

the affinity and reactivity of the present active site, as the reactivity of each site increased from 3 ions by KA to 5 by EXK and 10 by KNTs. The very high reactivity of KNTs might be attributed to their enhanced dispersion properties, interaction interface, and reactivity of the surface to induce the aggregation of the metal ions during their uptake by their active chemical groups.

In terms of temperature effects, the computed $n_{(Cs^+)}$ values also demonstrate the significant impact of the morphological changes on the surficial features of the aluminosilicate units, as the three structures (KA, EXK, and KNTs) display different behaviors. For KA, the reported values of $n_{(Cs^+)}$ in terms of temperature show slight fluctuation as the value decreased by rising from 298 K ($n_{(Cs^+)} = 3.8$) to 308 K ($n_{(Cs^+)} = 3.6$) and then increased again as the temperature rose to 313 K ($n_{(Cs^+)} = 3.9$) (Table 3 and Fig. 8D). For KNTs, the behavior was reversed as the results exhibited a positive correlation with the ambient temperature, particularly from 298 K ($n_{(Cs^+)} = 5.3$) to 308 K ($n_{(Cs^+)} = 9.13$), and then declined again as the temperature attained 313 K ($n_{(Cs^+)} = 8.44$) (Table 3 and Fig. 8F). The observed behavior can potentially be attributed to changes in the quantity, activation, and types of the reactive functional receptors of $Cs^+$ ions with variations in temperature conditions.[1,56] However, the increment in temperature up to 308 K enhances the aggregation affinity of the $Cs^+$ ions during their adsorption by KNTs; this reduces their aggregation behaviors during their interaction with the surface of KA. Regarding the behavior of the values of $n_{(Cs^+)}$ with temperature for EXK, the estimated values validate observable declination as the testing temperature increases from 298 K ($n_{(Cs^+)} = 4.9$) up to 313 K ($n_{(Cs^+)} = 4.4$) (Table 3 and Fig. 8E). This was ascribed to the expected decrease in $Cs^+$ aggregation properties along the interface with the EXK surface during the interaction of the cesium ions with the kaolinite structure under high temperature conditions.[51]

*3.2.7.2. Occupied active sites density ($N_m$).* The density of cesium-filled positions was assessed ($N_{m(Cs^+)}$) in KA, EXK, and KNTs is indicative of the overall number of available binding sites across the surfaces of their particles throughout the reaction's duration. The $N_{m(Cs^+)}$ values obtained for KA are 19.4 mg g$^{-1}$ at 298 K, 17.8 mg g$^{-1}$ at 308 K, and 13 mg g$^{-1}$ at 313 K, as depicted in Fig. 8G. The values exhibited significant improvement following the implementation of exfoliation transformations (EXK), resulting in values of 40.8 mg g$^{-1}$ (298 K), 36.2 mg g$^{-1}$ (308 K), and 27.8 mg g$^{-1}$ (313 K) (Fig. 8H and Table 3). Additionally, following the silicate sheets' scrolling into nanotubes (KNTs), the active sites' accessibility significantly increased to 46.9 mg g$^{-1}$ (298 K), 22.6 mg g$^{-1}$ (308 K), and 20.6 mg g$^{-1}$ (313 K) (Fig. 8I and Table 3). The findings support a significant increase in the total number of reactive sites after the exfoliating alteration, resulting in the formation of individual nano-sheets and the subsequent rolling of the aforementioned structures into nanotubes with improved dispersion qualities. The primary factors contributing to this phenomenon are the increase in surface area, the prolonged exposing properties of the strongly reactive siloxane distinct groups and the silicate surface's heightened reactivity resulting from its transformation into semi-crystalline form or amorphous compounds. These changes facilitate the formation of a reaction interface facilitates the interaction of $Cs^+$ solutions with the external surfaces of EXK and KNTs.

Regarding the temperature influence, the recognized occupied active site density ($N_m$) by the retained cesium ions and the recognized behaviors demonstrate general diminishing with rising the testing temperature using KA as well as EXK and KNTs (Fig. 8G–I). This demonstrates the negative impact of elevated temperatures on the predominance of active positions and/or deactivation effects on the present sites and/or the contact time for the effective retention of the cesium ions by the existing sites. The previous studies demonstrated similar behaviors and assigned that to the predicted desorption of the sequestrated cesium ion on the surface of clay-based materials as the saturation levels of the heated solutions declined with successful uptake reactions.[57] For KA as well as KNTs, this is significantly in accordance with the established findings of $n_{(Cs^+)}$ and the aggregation behaviors. The increment in the aggregation affinities of the cesium ions resulted in a delineation in the number of occupied sites.[58] This relation between the $N_{m(Cs^+)}$ and $n_{(Cs^+)}$ values of EXK in terms of evaluating temperature was not detected, as the two parameters display the same behavior with temperature. These results suggested that the previously mentioned changes in the values of $n_{(Cs^+)}$ were affected mainly by the aggregation properties and interionic interactions of the cesium ions, rather than their interaction with the silicate surface or the existence or activation of the effective retention receptor with temperature.

*3.2.7.3. Adsorption capacity at the saturation state of ($Q_{sat}$).* The most accurate prediction of the maximum adsorption qualities can potentially be accomplished by analyzing the $Cs^+$ retention properties of KA, EXK, and KNTs while they are in

a saturated state ($Q_{sat}$). The outcomes of $Q_{sat}$ are significantly influenced by the identified both the fulfilled site quantities ($N_{m(Cs^+)}$) and the total quantity of $Cs^+$ ions gathered by single position ($n_{(Cs^+)}$). Kaolinite, being a possible adsorbent of $Cs^+$, exhibits established $Q_{sat}$ levels of 73.8 mg $g^{-1}$ at 298 K, 64.7 mg $g^{-1}$ at 308 K, and 50.6 mg $g^{-1}$ at 313 K (Fig. 8J and Table 3). The exfoliating product (EXK) exhibits better retention capacities at different temperatures. Specifically, at 298 K, the uptake capacity is up to 199.8 mg $g^{-1}$. At 308 K, the uptake capacity is 166.2 mg $g^{-1}$, and at 313 K, it is 122.3 mg $g^{-1}$ (Fig. 8K and Table 3). The detected enhancement experienced a substantial increase following the transformation of the layers into nanotubes (KNTs), resulting in values of 249.7 mg $g^{-1}$ (298 K), 209.5 mg $g^{-1}$ (308 K), and 174 mg $g^{-1}$ (313 K) (Fig. 8L and Table 3). The detrimental impacts of temperature eventually resulted in the conclusion that KA, EXK, and KNTs exhibit exothermic tendencies in their $Cs^+$ retention activities. This illustrated how the testing temperature has an acceleration effect on the retention's thermal collision characteristics, which lowers the effectiveness of $Cs^+$ binding.[55] Furthermore, the determined capacities of $Q_{sat}$ associated with variations in retention temperature are in light of the aforementioned characteristics exhibited by $N_{m(Cs^+)}$ *versus* $n_{(Cs^+)}$. This suggests that the availability of the active sites plays a crucial role in regulating the performance of $Cs^+$ adsorption, instead of the prospective capacity of individual active sites for KA and KNTs. However, it is important to note that both parameters do influence the adsorption capacity of cesium ions by EXK.

### 3.2.8. Energetic studies

*3.2.8.1. Uptake energy.* The determination of the energy changes ($\Delta E$) associated with the uptake activities of $Cs^+$ can provide valuable insights into the underlying mechanisms, whether they are governed by chemical or physical factors. Chemical pathways typically exhibit energy levels exceeding 80 kJ $mol^{-1}$, while physical reactions tend to possess energies below 40 kJ $mol^{-1}$. The mechanistic reactions that occur during physical processes can be classified into many types according to the values of adsorption energies. The mechanisms under consideration encompass hydrogen bonding (with an energy range of less than 30 kJ $mol^{-1}$), van der Waals attraction (ranging from 4 to 10 kJ $mol^{-1}$), dipole–dipole interactions (with energies ranging from 2 to 29 kJ $mol^{-1}$), coordination exchange (with an energy of 40 kJ $mol^{-1}$), and hydrophobic interactions (with an energy of 5 kJ $mol^{-1}$).[51,59] The computation and determination of the $Cs^+$ retention energy levels ($E$) have been accomplished using eqn (5), which incorporates the calculated solubility of $Cs^+$ in testing solutions ($S$), gas constant, $Cs^+$ levels when KA, EXK, and KNTs are a half saturated, and the temperature within absolute terms ($T$).[58]

$$\Delta E = RT \ln\left(\frac{S}{C}\right) \quad (5)$$

The computed energies for the immobilization of $Cs^+$ *via* KA and EXK fall inside the boundaries of −8.3 to −8.5 kJ $mol^{-1}$ and −8.5 to −8.7 kJ $mol^{-1}$, respectively. On the other hand, the expected levels for KNTs exhibit a range of −9.02 to −9.12 kJ $mol^{-1}$. Hence, the uptake of $Cs^+$ by KA, EXK, and KNTs primarily occurred by physical mechanisms involving dipole–dipole interactions (2 to 29 kJ $mol^{-1}$), van der Waals force (4 to 10 kJ $mol^{-1}$), and hydrogen bonding (<30 kJ $mol^{-1}$). Moreover, the observed negative values of $\Delta E$ for the $Cs^+$ capture reactions by KA, EXK, and KNTs are consistent with the findings from the tests conducted about the exothermic nature of these processes.

### 3.2.9. Thermodynamic aspects

*3.2.9.1. Entropy.* The order as well as disorder features of KA, EXK, and KNTs' particulates can be identified by the entropy ($S_a$) corresponding to the retention of $Cs^+$ by them when exposed to various levels of $Cs^+$ and temperature conditions. The $S_a$ aspects have been emphasized based on the earlier determined $N_m$ and $n$ quantities, as well as the $Cs^+$ contents throughout the half-saturation phases of KA, EXK, and KNTs ($C_{1/2}$).

$$\frac{S_a}{K_B} = N_m \left\{ \ln\left(1 + \left(\frac{C}{C_{1/2}}\right)^n\right) - n\left(\frac{C}{C_{1/2}}\right)^n \frac{\ln\left(\frac{C}{C_{1/2}}\right)}{1 + \left(\frac{C}{C_{1/2}}\right)^n} \right\} \quad (6)$$

The results obtained illustrate a significant drop in entropy magnitudes ($S_a$) when $Cs^+$ is absorbed by KA, EXK, and KNTs, particularly at high $Cs^+$ levels. The observed trends illustrate a significant diminution of the disorder aspects of the interfaces of KA, EXK, and KNTs as the levels of $Cs^+$ ions increase (see Fig. 9A–C). The observed entropy aspects additionally provide evidence for the successful docking of $Cs^+$ ions onto the pre-existing active sites of KA, EXK, and KNTs, besides the unoccupied binding receptors, at low levels of the existing cesium ions.[58,60] Throughout the retention of $Cs^+$ by KA, it was noted that at equilibrium levels of 86.48 mg $L^{-1}$ (298 K), 83.28 mg $L^{-1}$ (308 K), and 79.8 mg $L^{-1}$ (313 K), the maximum degree of entropy was attained (Fig. 9A). The corresponding equilibrium levels of greatest entropy, as determined for EXK, were found to be 70.88 mg $g^{-1}$ at 298 K, 63.7 mg $g^{-1}$ at 308 K, and 56.2 mg $g^{-1}$ at 313 K (Fig. 9B). The highest entropy levels during the utilization of KNTs as adsorbents for $Cs^+$ ions are 60.5 mg $L^{-1}$ (at a temperature of 298 K), 52.5 mg $L^{-1}$ (at a temperature of 308 K), and 47.3 mg $L^{-1}$ (at a temperature of 313 K) (Fig. 9C). The equilibrium levels closely correspond to the $Cs^+$ concentrations expected under the conditions for half-saturation for KA, EXK, and KNTs. Consequently, the binding sites of $Cs^+$ ions become unavailable for further docking. Moreover, the observed reductions in entropy values suggest a notable fall in the quantity of unoccupied sites, along with a discernible drop in the characteristics of freedom and mobility displayed by the $Cs^+$ ions.[61]

*3.2.9.2. Internal energy and free enthalpy.* The present study evaluates the internal energy ($E_{int}$) associated with the retention of $Cs^+$ ions by K, EXK, and KNTs. Additionally, the changes in free enthalpy ($G$) triggered by variations in the $Cs^+$-initiated concentrations along with the testing temperature are examined. The assessment is conducted using the parameters outlined in eqn (7) and (8), which are dependent on the previously

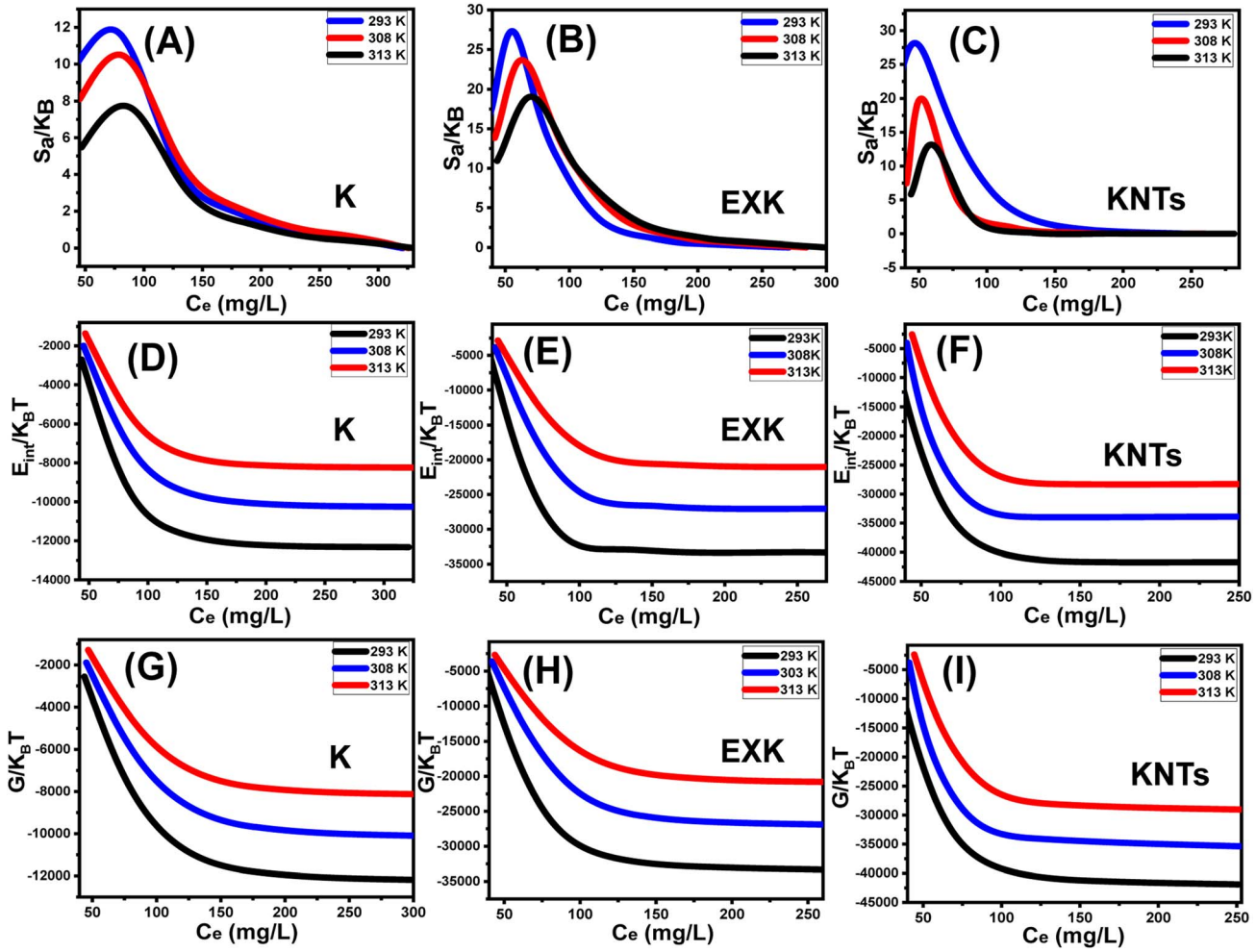


Fig. 9 The variation in entropy characteristics though the $Cs^+$ are being retained (KA (A), EXK (B), and KNTs (C)), variation in internal energy characteristics that occurs though $Cs^+$ are retained (KA (D), EXK (E), and KNTs (F)), and variation of the free enthalpy characteristics while the $Cs^+$ ions are being retained (KA (G), EXK (H), and KNTs (I)).

defined values of $N_m$, $n$, and $C_{1/2}$, as well as the translation partition ($Z_v$).[56]

$$\frac{E_{int}}{K_B T} = nN_m \left[ \left( \frac{\left(\frac{C}{C_{1/2}}\right)^n \ln\left(\frac{C}{Z_v}\right)}{1+\left(\frac{C}{C_{1/2}}\right)^n} \right) - \left( \frac{n \ln\left(\frac{C}{C_{1/2}}\right)\left(\frac{C}{C_{1/2}}\right)^n}{1+\left(\frac{C}{C_{1/2}}\right)^n} \right) \right] \quad (7)$$

$$\frac{G}{K_B T} = n\, N_m \frac{\ln\left(\frac{C}{Z_v}\right)}{1+\left(\frac{C_{1/2}}{C}\right)^n} \quad (8)$$

The determined values of internal energy ($E_{int}$) for adsorption reactions of $Cs^+$ on KA, EXK, and KNTs exhibit negative values. These results indicate a significant reduction in $E_{int}$ when the operating temperature is raised from 298 K to 313 K, as depicted in Fig. 9D–F. Consequently, the $Cs^+$ adsorption mechanisms of KA, EXK, and KNTs display a higher degree of spontaneity and exothermicity. Similar actions and features have been detected for the predefined enthalpy values, as depicted in Fig. 9G–I. The $G$ levels exhibit a negative trend and display reversible relationships with the evaluated temperature, suggesting a drop in the criteria of feasibility. This observation endorses the $Cs^+$ retention's exothermic and spontaneous belongs of KA, EXK, and KNTs, as depicted in Fig. 9G–I.

**3.2.10. Effect of coexisting ions.** A comprehensive experimental investigation was conducted to examine the potential adverse effects of various metal ions in addition to soluble anions on the binding capacity of synthetic KA, EXK, and KNTs for $Cs^+$ ions. The metals that were examined in this study were $Cd^{2+}$, $Zn^{2+}$, $Pb^{2+}$, and $Co^{2+}$, whereas the anions that were examined included $HCO_3^-$, $NO_3^-$, $SO_4^{2-}$, and $PO_4^{3-}$. The primary variables have been selected to have maintained values [incorporated dosage: 0.4 g $L^{-1}$; duration: 24 hours; tested volume: 100 mL; concentration: 100 mg $L^{-1}$ (50% $Cs^+$ + 50% the coexisting ion); temperature: 298 K]. All of the dissolved anions involved possess a very little effect on KA, EXK, and KNTs

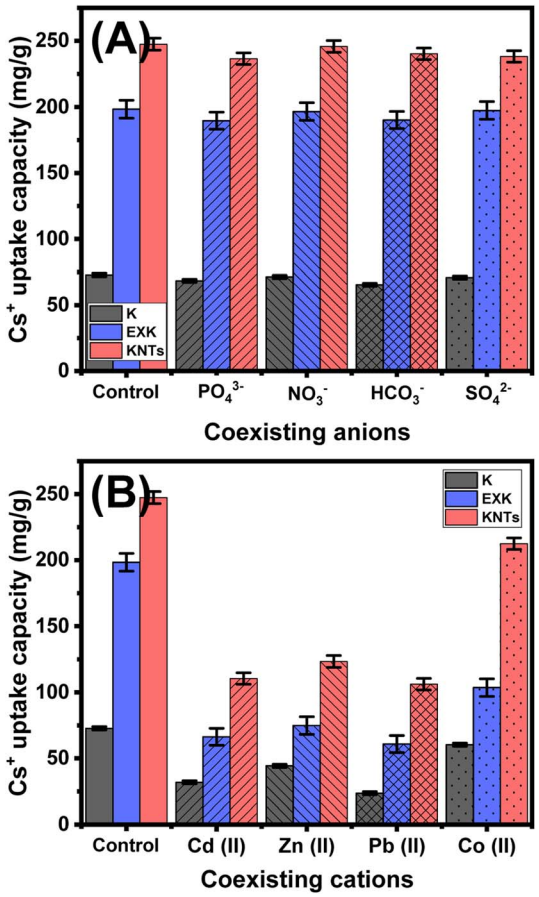


Fig. 10 Effect of the coexisting anions (A) and metal cations (B) on the uptake performances of KA, EXK, and KNTs for $Cs^+$ ions.

elimination sensitivity towards $Cs^+$ ions (Fig. 10). The soluble anions of $PO_4^{3-}$ and $HCO_3^-$ exhibited the most pronounced inhibitory impact on the retention activities of $Cs^+$ (Fig. 10A). The regulating mechanism, which involves ligand exchange along with complexation activities, may be used to illustrate this.[62,63] These two soluble anions ($PO_4^{3-}$ and $HCO_3^-$) have a tendency to create extremely stable inner complexes with their functional structures that possess active hydroxyl groups. This characteristic makes them very competitive with $Cs^+$ ions (Fig. 10A).[62–64] The other species of soluble anions, including $SO_4^{2-}$ and $NO_3^-$, have a tendency to develop into outer-sphere complexes that are of poor stability, and, as a consequence, they have limited competitive characteristics with the $Cs^+$ ions throughout the adsorption stages.[63]

The incorporation of other metallic ions, including $Cd^{2+}$, $Pb^{2+}$, and $Zn^{2+}$, has a significant negative impact on the uptake of $Cs^+$ ions. Likewise, the presence of $Co^{2+}$ ions has a significantly adverse impact on the sensitivities of KA, EXK, and KNTs for $Cs^+$ ions (Fig. 10B). However, the materials still have better performance for the examined cesium ions than cobalt ions (Fig. 10B). The synthetic EXK and KNTs nanostructures exhibit excellent effectiveness in eliminating cesium ions from water supplies, regardless of the presence of additional species of soluble chemicals, either anions or metallic cations, based on the concentration of $Cs^+$ ions that were examined.

**3.2.11. Recyclability.** The reusability tests were conducted in order to assess the suitability of synthesized EXK and KNTs for use in commercial and industrial-scale operations. The process of regenerating the EXK and KNT particulates included subjecting them to a washing procedure using a dilute solution of $NH_4Cl$ (1 mol $L^{-1}$) for a duration of 10 minutes. This was done with the aid of a magnetic stirrer to ensure efficient elution along with the desorption of the binding $Cs^+$ ions. Subsequently, the particles underwent separation by filtering and were subjected to an extra washing process using distilled water for duration of 10 minutes. Following this, the particulates were dried for a period of 10 hours at a temperature of 60 °C to get ready for their utilization in the subsequent adsorption cycles (Fig. 11). The experiment was conducted in five replicates, considering the elimination capacity of $Cs^+$ ions. The parameters that were adjusted throughout the experiment were the solid dose (0.4 g $L^{-1}$), length (24 hours), volume (100 mL), concentration (100 mg $L^{-1}$), and temperature (298 K). The experimental findings regarding the elimination efficiency of $Cs^+$ ions indicate that EXK and KNTs exhibit favorable stability as adsorbents with notable recyclability potential. In terms of the recycling of EXK throughout the sequestration of $Cs^+$ ions, the material exhibited a removal capacity over 197 mg $g^{-1}$ for two cycles, exceeding 195 mg $g^{-1}$ for three cycles, and exceeding 185 mg $g^{-1}$ throughout five cycles (Fig. 11). Throughout the recyclability of KNTs during the elimination of $Cs^+$ ions, the reported elimination capacities exceed 245 mg $g^{-1}$ during two cycles, surpass 240 mg $g^{-1}$ throughout three cycles, and exceed 230 mg $g^{-1}$ throughout five cycles (Fig. 11). The observed linear decline in the effectiveness of the elimination of $Cs^+$ ions by the EXK and KNTs materials as the reuse and recycling cycles increase may be attributed to the persistent creation of complexes between the cesium ions and the structural reactive groups of EXK and KNTs. These complexes development leads to a decrease in the number of accessible, unoccupied sites for adsorption.

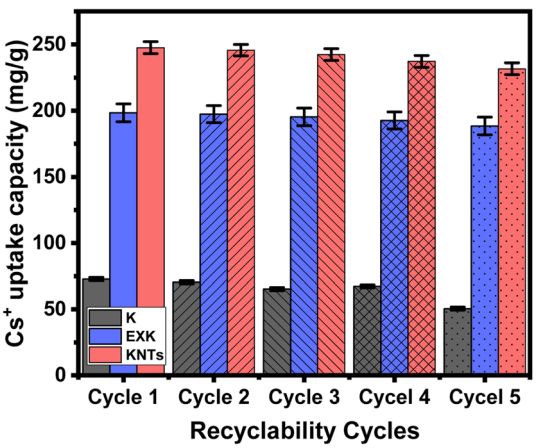


Fig. 11 The recyclable potential of KA, EXK, and KNTs during the retention of $Cs^+$ ions.

## 4 Conclusion

The retention performances of $Cs^+$ ions by synthetic exfoliated nano-kaolinite sheets (EXK) and kaolinite nanotubes (KNTs) were assessed as advanced, eco-friendly, clay-based adsorbents of controlled morphologies. The scrolled products display the best retention capacity of $Cs^+$ (249.7 mg $g^{-1}$) as compared to the EXK product (199.8 mg $g^{-1}$) and the raw kaolinite (73.8 mg $g^{-1}$). The sequestration mechanism in terms of the adsorbents/$Cs^+$ interfaces was described according to the scientific significance of the advanced monolayer isotherm model. The steric investigations revealed a significant increase in the number of currently available active sites of adsorption from 9.4 mg $g^{-1}$ for kaolinite to 40.8 mg $g^{-1}$ for EXK and 46.9 mg $g^{-1}$ for KNTs at 298 K in consequence of the rise in surface area and subsequent augmentation in surface reactivity. This enhancement in reactivity appeared in the increment in the number of retained $Cs^+$ ions ($n$ = 10 (KNTs) and 5 (EXK)), which also suggested multi-ionic mechanisms. The determined retention energies (<40 kJ $mol^{-1}$) and the estimated thermodynamic functions reflect the exothermic, physical, and spontaneous sequestration of $Cs^+$ by EXK and KNTs. Finally, the two structures display considerable elimination performance of the $Cs^+$ ion even in the co-existence of additional metal ions or chemical anions.

## Conflicts of interest

There are no conflicts to declare.

## Acknowledgements

The authors extend their appreciation to the Deputyship for Research & Innovation, Ministry of Education in Saudi Arabia for funding this research through the project number IFP-IMSIU-2023125. The authors also appreciate the Deanship of Scientific Research at Imam Mohammad Ibn Saud Islamic University (IMSIU) for supporting and supervising this project.

## References

1 X. Yang, J. Wang, A. M. El-Sherbeeny, A. A. AlHammadi, W.-H. Park and M. R. Abukhadra, Insight into the adsorption and oxidation activity of a ZnO/piezoelectric quartz core-shell for enhanced decontamination of ibuprofen: steric, energetic, and oxidation studies, *Chem. Eng. J.*, 2022, **431**, 134312.

2 M. A. Salam, M. Mokhtar, S. M. Albukhari, D. F. Baamer, L. Palmisano, M. Jaremko and M. R. Abukhadra, Synthesis and Characterization of Green ZnO@ polynaniline/Bentonite Tripartite Structure (G. Zn@ PN/BE) as Adsorbent for As (V) Ions: Integration, Steric, and Energetic Properties, *Polymers*, 2022, **14**(12), 2329.

3 M. R. Abukhadra, M. Mostafa, M. N. B. Jumah, N. Al-Khalawi, R. S. Alruhaimi, Y. F. Salama and A. A. Allam, Correction: Insight into the Adsorption Properties of Chitosan/Zeolite-A Hybrid Structure for Effective Decontamination of Toxic Cd (II) and As (V) Ions from the Aqueous Environments, *J. Polym. Environ.*, 2022, **30**, 4500.

4 I. R. Sayed, A. M. Farhan, A. A. AlHammadi, M. I. El-Sayed, I. M. Abd El-Gaied, A. M. El-Sherbeeny, W. Al Zoubi, Y. G. Ko and M. R. Abukhadra, Synthesis of novel nanoporous zinc phosphate/hydroxyapatite nano-rods (ZPh/$HPA_{NRs}$) core/shell for enhanced adsorption of $Ni^{2+}$ and $Co^{2+}$ ions: characterization and application, *J. Mol. Liq.*, 2022, **360**, 119527.

5 F. Javaheri, Z. Kheshti, S. Ghasemi and A. Altaee, Enhancement of $Cd^{2+}$ removal from aqueous solution by multifunctional mesoporous silica: equilibrium isotherms and kinetics study, *Sep. Purif. Technol.*, 2019, **224**, 199–208.

6 S. Kang, J. Lee, S. M. Park, D. S. Alessi and K. Baek, Adsorption characteristics of cesium onto calcium-silicate-hydrate in concrete powder and block, *Chemosphere*, 2020, **259**, 127494.

7 S. J. Park, S. S. Shin, J. H. Jo, C. H. Jung, H. Park, Y. I. Park, H. J. Kim and J. H. Lee, Tannic acid-assisted in situ interfacial formation of Prussian blue-assembled adsorptive membranes for radioactive cesium removal, *J. Hazard Mater.*, 2023, **442**, 129967.

8 M. A. Salam, M. R. Abukhadra and M. Mostafa, Effective decontamination of As (V), Hg (II), and U (VI) toxic ions from water using novel muscovite/zeolite aluminosilicate composite: adsorption behavior and mechanism, *Environ. Sci. Pollut. Res.*, 2020, **27**(12), 13247–13260.

9 B. S. Reddy, A. K. Maurya, V. E. Sathishkumar, P. L. Narayana, M. H. Reddy, A. Baazeem, K. K. Cho and N. S. Reddy, Prediction of batch sorption of barium and strontium from saline water, *Environ. Res.*, 2021, **197**, 111107.

10 B. Park, S. M. Ghoreishian, Y. Kim, B. J. Park, S. M. Kang and Y. S. Huh, Dual-functional micro-adsorbents: application for simultaneous adsorption of cesium and strontium, *Chemosphere*, 2021, **263**, 128266.

11 H. M. Saleh, H. R. Moussa, F. A. El-Saied, M. Dawoud, A. N. El Said and R. S. A. Wahed, Adsorption of cesium and cobalt onto dried Myriophyllum spicatum L. from radio- contaminated water: experimental and theoretical study, *Prog. Nucl. Energy*, 2020, **125**, 103393.

12 A. M. Emara, E. M. Elsharma and I. M. Abdelmonem, Adsorption of radioactive cesium using synthesized chitosan-g-poly (acrylic acid/N-vinylcaprolactam) by γ-irradiation, *Radiat. Phys. Chem.*, 2023, **208**, 110892.

13 Q. T. N. Le and K. Cho, Caesium adsorption on a zeolitic imidazolate framework (ZIF-8) functionalized by ferrocyanide, *J. Colloid Interface Sci.*, 2021, **581**, 741–750.

14 H. Seema, N. Khan and A. Muhammad, Fabrication of self-assembled Prussian blue graphene hydrogel for highly selective removal of radioactive cesium in water: Adsorption study, *Mater. Chem. Phys.*, 2023, **306**, 128003.

15 S. Kwon, Y. Kim and Y. Roh, Cesium removal using acid-and base-activated biotite and illite, *J. Hazard. Mater.*, 2021, **401**, 123319.

16 O. Falyouna, O. Eljamal, I. Maamoun, A. Tahara and Y. Sugihara, Magnetic zeolite synthesis for efficient

removal of cesium in a lab-scale continuous treatment system, *J. Colloid Interface Sci.*, 2020, **571**, 66–79.

17 W. Wang, L. Shi, H. Wu, Z. Ding, J. Liang, P. Li and Q. Fan, Interactions between micaceous minerals weathering and cesium adsorption, *Water Res.*, 2023, **238**, 119918.

18 H. Wi, H. Kim, D. Oh, S. Bae and Y. Hwang, Surface modification of poly (vinyl alcohol) sponge by acrylic acid to immobilize Prussian blue for selective adsorption of aqueous cesium, *Chemosphere*, 2019, **226**, 173–182.

19 J. Wang and S. Zhuang, Removal of cesium ions from aqueous solutions using various separation technologies, *Rev. Environ. Sci. Bio/Technol.*, 2019, **18**, 231–269.

20 B. Isık, A. E. Kurtoğlu, G. Gürdağ and G. Keçeli, Radioactive cesium ion removal from wastewater using polymer metal oxide composites, *J. Hazard. Mater.*, 2021, **403**, 123652.

21 Y. Zhang, Y. Xiong, Q. Xian, X. He, H. Dan and Y. Ding, Efficient adsorption and in situ solidification of cesium from aqueous solution using mesoporous MnO2@ SBA-15, *Ann. Nucl. Energy*, 2023, **180**, 109509.

22 S. Khandaker, Y. Toyohara, S. Kamida and T. Kuba, Adsorptive removal of cesium from aqueous solution using oxidized bamboo charcoal, *Water Resour. Ind.*, 2018, **19**, 35–46.

23 C. Dong, X. Deng, X. Guo, B. Wang, X. Ye, J. Fan, C. Zhu, F. Fan and B. Qing, Synthesis of potassium metal ferrocyanide/Al-MCM-41 with fast and selective adsorption of cesium, *Colloids Surf., A*, 2021, **613**, 126107.

24 T. Abdollahi, J. Towfighi and H. Rezaei-Vahidian, Sorption of cesium and strontium ions by natural zeolite and management of produced secondary waste, *Environ. Technol. Innov.*, 2020, **17**, 100592.

25 M. R. Abukhadra, I. Saad, S. I. Al Othman, H. E. Alfassam and A. A. Allam, Insight into the synergetic, steric and energetic properties of zeolitization and cellulose fiber functionalization of diatomite during the adsorption of Cd (ii): advanced equilibrium studies, *RSC Adv.*, 2023, **13**(34), 23601–23618.

26 M. R. Abukhadra, A. AlHammadi, A. M. El-Sherbeeny, M. A. Salam, M. A. El-Meligy, E. M. Awwad and M. Luqman, Enhancing the removal of organic and inorganic selenium ions using an exfoliated kaolinite/cellulose fibres nanocomposite, *Carbohydr. Polym.*, 2021, **252**, 117163.

27 H. Çiftçi, Removal of methylene blue from water by ultrasound-assisted adsorption using low-cost bentonites, *Chem. Phys. Lett.*, 2022, **802**, 139758.

28 M. D. Alqahtani, N. Nasser, M. N. Bin Jumah, S. A. AlZahrani, A. A. Allam, M. R. Abukhadra and S. Bellucci, Insight into the Morphological Properties of Nano-Kaolinite (Nanoscrolls and Nanosheets) on Its Qualification as Delivery Structure of Oxaliplatin: Loading, Release, and Kinetic Studies, *Molecules*, 2023, **28**(13), 5158.

29 L. Tian, M. R. Abukhadra, A. S. Mohamed, A. Nadeem, S. F. Ahmad and K. E. Ibrahim, Insight into the loading and release properties of an exfoliated kaolinite/cellulose fiber (EXK/CF) composite as a carrier for oxaliplatin drug: cytotoxicity and release kinetics, *ACS Omega*, 2020, **5**(30), 19165–19173.

30 M. Shaban, M. I. Sayed, M. G. Shahien, M. R. Abukhadra and Z. M. Ahmed, Adsorption behavior of inorganic-and organic-modified kaolinite for Congo red dye from water, kinetic modeling, and equilibrium studies, *J. Sol-Gel Sci. Technol.*, 2018, **87**(2), 427–441.

31 M. R. Abukhadra, M. Mostafa, A. M. El-Sherbeeny, M. A. El-Meligy and A. Nadeem, Instantaneous adsorption of synthetic dyes from an aqueous environment using kaolinite nanotubes: equilibrium and thermodynamic studies, *ACS Omega*, 2021, **6**(1), 845–856.

32 M. I. Carretero and M. Pozo, Clay and non-clay minerals in the pharmaceutical and cosmetic industries part II. Active ingredients, *Appl. Clay Sci.*, 2010, **47**(3–4), 171–181.

33 M. R. Abukhadra and A. F. Allah, Synthesis and characterization of kaolinite nanotubes (KNTs) as a novel carrier for 5-fluorouracil of high encapsulation properties and controlled release, *Inorg. Chem. Commun.*, 2019, **103**, 30–36.

34 A. M. Saad, M. R. Abukhadra, S. A. K. Ahmed, A. M. Elzanaty, A. H. Mady, M. A. Betiha, J. J. Shim and A. M. Rabie, Photocatalytic degradation of malachite green dye using chitosan supported ZnO and Ce–ZnO nano-flowers under visible light, *J. Environ. Manag.*, 2020, **258**, 110043.

35 J. H. Seo, M. Y. Lee and J. S. Kim, Radio-frequency thermal plasma preparation of nano-sized Ni catalysts supported on MgO nano-rods for partial oxidation of methane, *Surf. Coat. Technol.*, 2013, **228**, S91–S96.

36 R. Sabry and O. AbdulAzeez, Hydrothermal growth of ZnO nano rods without catalysts in a single step, *Manuf. Lett.*, 2014, **2**(2), 69–73.

37 R. Singh and S. Dutta, The role of pH and nitrate concentration in the wet chemical growth of nano-rods shaped ZnO photocatalyst, *Nano-Struct. Nano-Objects*, 2019, **18**, 100250.

38 M. R. Abukhadra, B. M. Bakry, A. Adlii, S. M. Yakout and M. E. El-Zaidy, Facile conversion of kaolinite into clay nanotubes (KNTs) of enhanced adsorption properties for toxic heavy metals ($Zn^{2+}$, $Cd^{2+}$, $Pb^{2+}$, and $Cr^{6+}$) from water, *J. Hazard Mater.*, 2019, **374**, 296–308.

39 E. R. Adly, M. S. Shaban, A. M. El-Sherbeeny, W. Al Zoubi and M. R. Abukhadra, Enhanced Congo Red Adsorption and Photo-Fenton Oxidation over an Iron-Impeded Geopolymer from Ferruginous Kaolinite: Steric, Energetic, Oxidation, and Synergetic Studies, *ACS Omega*, 2022, **7**, 31218–31232.

40 A. Shawky, S. M. El-Sheikh, M. N. Rashed, S. M. Abdo and T. I. El-Dosoqy, Exfoliated kaolinite nanolayers as an alternative photocatalyst with superb activity, *J. Environ. Chem. Eng.*, 2019, **7**(3), 103174.

41 E. L. Vivas and K. Cho, Efficient adsorptive removal of cobalt (II) ions from water by dicalcium phosphate dihydrate, *J. Environ. Manag.*, 2021, **283**, 111990.

42 M. A. Salam, M. R. Abukhadra and M. Mostafa, Effective decontamination of As (V), Hg (II), and U (VI) toxic ions from water using novel muscovite/zeolite aluminosilicate

composite: adsorption behavior and mechanism, *Environ. Sci. Pollut. Res.*, 2020, **27**(12), 13247–13260.

43 Y. Jiang, M. R. Abukhadra, N. M. Refay, M. F. Sharaf, M. A. El-Meligy and E. M. Awwad, Synthesis of chitosan/MCM-48 and β-cyclodextrin/MCM-48 composites as bio-adsorbents for environmental removal of Cd2+ ions; kinetic and equilibrium studies, *React. Funct. Polym.*, 2020, **154**, 104675.

44 A. M. El-Sherbeeny, S. M. Ibrahim, A. A. AlHammadi, A. T. A. Soliman, J. J. Shim and M. R. Abukhadra, Effective retention of radioactive $Cs^{+}$ and $Ba^{2+}$ ions using β-cyclodextrin functionalized diatomite (β-CD/D) as environmental adsorbent; characterization, application, and safety, *Surf. Interfaces*, 2021, **26**, 101434.

45 E. El Qada, Kinetic Behavior of the Adsorption of Malachite Green Using Jordanian Diatomite as Adsorbent, *Jordanian J. Eng. Chem. Ind.*, 2020, **3**(1), 1–10.

46 X. Lin, Y. Xie, H. Lu, Y. Xin, R. Altaf, S. Zhu and D. Liu, Facile preparation of dual La-Zr modified magnetite adsorbents for efficient and selective phosphorus recovery, *Chem. Eng. J.*, 2021, **413**, 127530.

47 S. M. Albukhari, M. A. Salam and M. R. Abukhadra, Effective retention of inorganic selenium ions (Se (VI) and Se (IV)) using novel sodalite structures from muscovite; characterization and mechanism, *J. Taiwan Inst. Chem. Eng.*, 2021, **120**, 116–126.

48 A. Sherlala, A. Raman, M. M. Bello and A. Buthiyappan, Adsorption of arsenic using chitosan magnetic graphene oxide nanocomposite, *J. Environ. Manag.*, 2019, **246**, 547–556.

49 Y. Huang, X. Zeng, L. Guo, J. Lan, L. Zhang and D. Cao, Heavy metal ion removal of wastewater by zeolite-imidazolate frameworks, *Sep. Purif. Technol.*, 2018, **194**, 462–469.

50 E. E. Jasper, V. O. Ajibola and J. C. Onwuka, Nonlinear regression analysis of the sorption of crystal violet and methylene blue from aqueous solutions onto an agro-waste derived activated carbon, *Appl. Water Sci.*, 2020, **10**(6), 1–11.

51 M.-T. Ashraf, A. A. AlHammadi, A. M. El-Sherbeeny, S. Alhammadi, W. Al Zoubi, Y. G. Ko and M. R. Abukhadra, Synthesis of cellulose fibers/zeolite-A nanocomposite as an environmental adsorbent for organic and inorganic selenium ions; characterization and advanced equilibrium studies, *J. Mol. Liq.*, 2022, **360**, 119573.

52 M. R. Abukhadra, F. M. Dardir, M. Shaban, E. A. Ahmed and M. F. Soliman, Superior removal of $Co^{2+}$, $Cu^{2+}$ and $Zn^{2+}$ contaminants from water utilizing spongy Ni/Fe carbonate–fluorapatite; preparation, application and mechanism, *Ecotoxicol. Environ. Saf.*, 2018, **157**, 358–368.

53 M. Shaban, M. R. Abukhadra, M. G. Shahien and A. A. P. Khan, Upgraded modified forms of bituminous coal for the removal of safranin-T dye from aqueous solution, *Environ. Sci. Pollut. Res.*, 2017, **24**(22), 18135–18151.

54 F. Dawodu, G. Akpomie and M. Abuh, Equilibrium Isotherm Studies on the Batch Sorption of Copper (II) ions from Aqueous Solution unto Nsu Clay, *Int. J. Sci. Eng. Res.*, 2012, **3**(12), 1–7.

55 M. Mobarak, R. A. Ali and M. K. Seliem, Chitosan/activated coal composite as an effective adsorbent for Mn (VII): modeling and interpretation of physicochemical parameters, *Int. J. Biol. Macromol.*, 2021, **186**, 750–758.

56 F. Dhaouadi, L. Sellaoui, H. E. Reynel-Ávila, V. Landín-Sandoval, D. I. Mendoza-Castillo, J. E. Jaime-Leal, E. C. Lima, A. Bonilla-Petriciolet and A. B. Lamine, Adsorption mechanism of $Zn^{2+}$, $Ni^{2+}$, $Cd^{2+}$, and $Cu^{2+}$ ions by carbon-based adsorbents: interpretation of the adsorption isotherms via physical modelling, *Environ. Sci. Pollut. Res.*, 2021, **28**(24), 30943–30954.

57 S. Kubilay, R. Gürkan, A. Savran and T. Şahan, Removal of Cu (II), Zn (II) and Co (II) ions from aqueous solutions by adsorption onto natural bentonite, *Adsorption*, 2007, **13**, 41–51.

58 F. Dhaouadi, L. Sellaoui, M. Badawi, H. E. Reynel-Ávila, D. I. Mendoza-Castillo, J. E. Jaime-Leal, A. Bonilla-Petriciolet and A. B. Lamine, Statistical physics interpretation of the adsorption mechanism of $Pb^{2+}$, $Cd^{2+}$ and $Ni^{2+}$ on chicken feathers, *J. Mol. Liq.*, 2020, **319**, 114168.

59 R. A. Ali, M. Mobarak, A. M. Badawy, E. C. Lima, M. K. Seliem and H. Ramadan, New insights into the surface oxidation role in enhancing Congo red dye uptake by Egyptian ilmenite ore: Experiments and physicochemical interpretations, *Surf. Interfaces*, 2021, **26**, 101316.

60 L. Sellaoui, J. Ali, M. Badawi, A. Bonilla-Petriciolet and Z. Chen, Understanding the adsorption mechanism of $Ag^{+}$ and $Hg^{2+}$ on functionalized layered double hydroxide via statistical physics modeling, *Appl. Clay Sci.*, 2020, **198**, 105828.

61 L. Sellaoui, H. Guedidi, L. Reinert, S. Knani, L. Duclaux and A. B. Lamine, Experimental and theoretical studies of adsorption of ibuprofen on raw and two chemically modified activated carbons: new physicochemical interpretations, *RSC Adv.*, 2016, **6**(15), 12363–12373.

62 W. Shi, Y. Fu, W. Jiang, Y. Ye, J. Kang, D. Liu, Y. Ren, D. Li, C. Luo and Z. Xu, Enhanced phosphate removal by zeolite loaded with Mg–Al–La ternary (hydr) oxides from aqueous solutions: performance and mechanism, *Chem. Eng. J.*, 2019, **357**, 33–44.

63 Y. Yin, T. Zhou, H. Luo, J. Geng, W. Yu and Z. Jiang, Adsorption of arsenic by activated charcoal coated zirconium-manganese nanocomposite: performance and mechanism, *Colloids Surf., A*, 2019, **575**, 318–328.

64 C. C. Fu, H. N. Tran, X. H. Chen and R. S. Juang, Preparation of polyaminated Fe3O4@ chitosan core-shell magnetic nanoparticles for efficient adsorption of phosphate in aqueous solutions, *J. Ind. Eng. Chem.*, 2020, **83**, 235–246.